

# Signatures of Four Fermion Contact Couplings of a Dark Fermion and an Electron at Hadron Collider

Kai Ma<sup>a†</sup>

<sup>a</sup>*Department of Physics, Shaanxi University of Technology, Hanzhong 723000, Shaanxi, China*

## ABSTRACT

Both the collider searches and direct detections are promising approaches to probe a fermionic dark matter. In this paper we study signatures of the four fermion contact operators involving a dark fermion, an electron and a quark pair. We show that the mono-electron production channel at hadron collider can provide strong constraints. Associated productions of a charged electron with a photon/jet with missing energy are also studied. Using the current LHC data at  $\sqrt{s} = 13$  TeV, the lower bound on the energy scale of the (axial-)vector operator can reach to 12 TeV for a massless dark fermion. It can be further improved to about 24 TeV at the HE-LHC with  $\sqrt{s} = 25$  TeV and a total luminosity  $20 \text{ ab}^{-1}$ . For the direct detections, the signal operators can generate induced  $\beta^\pm$  decays. For the induced  $\beta^-$  decay, we show that the constraints are weaker than the ones from the collider searches in almost all of the parameter space, and the accessible parameter space is already excluded by the current LHC data. In case of a relative heavy dark fermion (a few MeV), the induced  $\beta^+$  decay is more sensitive than the collider search. Despite the advantage of the collider search that a much wider range of the dark fermion mass can be investigated, it can also provide a complementarity to the detect detections.

---

<sup>†</sup>[makai@ucas.ac.cn](mailto:makai@ucas.ac.cn)

# Contents

<b>1. Introduction.....</b>	<b>2</b>
<b>2. Effective Operators.....</b>	<b>4</b>
<b>3. Constraints at the LHC.....</b>	<b>5</b>
3.1. Mono-Lepton Production .....	5
3.2. Associated Production of Lepton with Photon.....	8
3.3. Associated Production of Lepton with Jet .....	12
3.4. Constraints at Future Hadron Colliders .....	16
<b>4. Induced <math>\beta</math> Decay .....</b>	<b>17</b>
4.1. Induced $\beta^-$ Decay .....	19
4.2. Induced $\beta^+$ Decay .....	22
<b>5. Conclusion .....</b>	<b>23</b>
<b>A. Nucleon Level Squared Amplitudes .....</b>	<b>25</b>

## 1 Introduction

The astrophysical and cosmological evidences of the Dark Matter (DM) [1–3] have inspired lots of experimental searches for its physical properties beyond the gravitational effects. Interactions between the DM and the Standard Model (SM) particles can be searched for indirectly by observing signals of its annihilations into the SM particles in high density regions of the universe [4, 5]. For instance, the significant signals of anomalous lepton and photon flux can be generated via the DM annihilation [6–10]. However, so far we have not observed any signal beyond its gravitational interaction [11–13].

Alternatively, the DM can also be searched for by scattering of the DM off nucleus [14–17], electrons [18] and phonons [19] of atom targets in terrestrial experiments, which are also called direct detections of the DM [20–22]. The scattering processes can be either elastic or inelastic. The elastic scattering off nucleus have provided strong constraints on the interactions between the nucleon and the DM with mass in the GeV–TeV range [23]. In case of that the DM has more than one particle components, mass gap(s) of the DM particles can be converted into kinematical energy of the final states. Such inelastic scattering can explore both heavy and light DM particles as long as the mass gap is sizable. Nevertheless, inelastic scattering can also happen for a single DM particle, which is call the absorption process [16–18] by which the DM is converted to a SM neutrino by the targets, and its DM mass completely transferred to the final states. Hence it is naturally sensitive to light DM particles. On the other hand, the DM can also be explored at colliders [22, 24–27].

Since the DM should couple to the known particles very weakly, and hence is represented as missing energy at colliders, the collider search usually looks for signals in large missing energy region. The advantage of this approach is that a much wider range of the DM mass can be investigated, the only restriction is the center of mass energy of the collider. This superiority is essentially promising for heavy dark particles which are usually predicted in the UV completed models of the dark sector.

While the direct detections and collider searches are completely different mechanism of hunting for the DM particle, they are strongly correlated in an evitable way. The hadron level operators which induce the DM scattering off the atom target have to be matched to the parton level interactions which are responsible to its direct production at colliders [24–27]. Therefore combined analysis of these two approaches is essential to have a proper and complementary constraints on the model parameters [28, 29]. In case of that stability of the DM is preserved by some discrete symmetry such as  $\mathbb{Z}_2$ , elastic scattering with a small mass and inelastic scattering with a much larger mass can be sizable in direct detection experiments, and at colliders the DM particles are produced in pair. In contrast, if the DM is always accompanied by a neutrino in interactions with the other known particles, the most sensitive channel in direction detections is the absorption process [14–18], and missing energy at collider is made up of the DM and a neutrino. Even though they have the same final state topology [17, 30, 31], kinematic properties of the missing energy can be significantly different [28]. As a result, constraints on the model parameters can be essentially different, particularly the combined constraints of the direct detections and collider searches. Furthermore, the DM can also be stable to have the correct relic abundance if it is light enough such that its decay width is considerably small [28, 32].

The DM-neutrino couplings to matter particles have been extensively studied. Here we focus on the case of that the dark fermion is always accompanied by a charged lepton. These two different kinds of interactions have distinctive signals in both the direct detection and collider search experiments. For instances, the DM-lepton couplings can simulate induced beta decay in direction detections, and mono-lepton production and associated productions of a lepton with either an energetic photon or one jet at hadron colliders. In the effective field theory (EFT) framework, the lowest order interactions with the matter particle are described by the four fermion contact operators. The four fermion contact couplings involving DM-neutrino and lepton pair are equivalent by Fierz transformation to the ones involving the DM-lepton and lepton-neutrino. Hence, in this paper we focus on phenomenologies of the four fermion contact couplings of the DM-lepton pair to a quark pair. We will study the details in both the direct detection and collider search experiments, as well as their combinations.

The rest of this paper is organized as follows. In Sec. 2, we discuss the essential properties of the charged four fermion contact interactions. In Sec. 3, we study signal properties of the mono-lepton process and associated production of a lepton with either a photon or a jet, as well as constraints from the current LHC data. Details of the mono- $\ell$ ,  $\ell\gamma$  and  $\ell j$  productions are given in the subsections 3.1, 3.2 and 3.3, respectively. Sensitivities which can be reached at HE-LHC are studied in the subsection 3.4. Constraints from direct detections in induced  $\beta$ -decay is studied in Sec. 4. Our conclusions are given in Sec. 5.

## 2 Effective Operators

For a fermionic dark particle, the effective interaction operator involving matter particles can be simply described at the lowest order by four fermion contact operators [30, 31, 33, 34]. In case of that the dark fermion couples to quarks in pair due to symmetry conservation, signals can be searched for either via elastic scattering of the dark fermion off nuclei in atoms [14], or through mono- $X$  ( $X = \gamma, Z/W$  and jets, etc) production at hadron colliders [35–38]. On the other hand, the dark fermion can come into play via mixing with the neutrino [16, 17]. The neutral current formed by the dark fermion-neutrino pair can induce inelastic scattering via absorption of the dark fermion by the nuclear target [16, 17, 39]. Apart from the neutral current, the dark fermion can also couple to quark pair via charged current formed by the dark fermion and the charged leptons [16, 17]. These couplings have nontrivial signals. For instance, the charged current can have significant contribution in the inverse  $\beta$ -decay [16, 17]. Here we focus on the four fermion contact operators formed by a dark fermion, a charged lepton and a quark pair.

The general four fermion contact interaction operators can be found in Ref. [40]. However, in consideration of that the possible mixing effect between the dark fermion and the neutrino can be easily taken into account for UV completed model building [17, 18, 39], we simply assume that the charged lepton (which is in the same isospin doublet with the neutrino) is left handed. And in contrast, for generality we do not put any prerequisite on chirality of the quark fields. Within this assumption, the EFT interaction Lagrangian can be explicitly written as,

$$\begin{aligned}
-\mathcal{L}_S &= \frac{1}{\Lambda_S^2} \mathcal{O}_S \equiv \frac{1}{\Lambda_S^2} [\bar{d}u] [\bar{\chi} \gamma_L \ell], \\
-\mathcal{L}_P &= \frac{1}{\Lambda_P^2} \mathcal{O}_P \equiv \frac{1}{\Lambda_P^2} [\bar{d}(i\gamma_5)u] [\bar{\chi} \gamma_L \ell], \\
-\mathcal{L}_V &= \frac{1}{\Lambda_V^2} \mathcal{O}_V \equiv \frac{1}{\Lambda_V^2} [\bar{d}\gamma_\mu u] [\bar{\chi} \gamma^\mu \gamma_L \ell], \\
-\mathcal{L}_A &= \frac{1}{\Lambda_A^2} \mathcal{O}_A \equiv \frac{1}{\Lambda_A^2} [\bar{d}\gamma_\mu \gamma_5 u] [\bar{\chi} \gamma^\mu \gamma_L \ell], \\
-\mathcal{L}_T &= \frac{1}{\Lambda_T^2} \mathcal{O}_T \equiv \frac{1}{\Lambda_T^2} [\bar{d}\sigma_{\mu\nu} u] [\bar{\chi} \sigma^{\mu\nu} \gamma_L \ell],
\end{aligned} \tag{2.1}$$

where  $\Lambda_i$  are independent energy scales characterizing possible fundamental new physics related to the corresponding operators  $\mathcal{O}_i$ . The above parameterization is complete in the sense of that all the five independent Lorentz structures for the quark bilinear are taken into account.

Since running effect of the EFT operators defined in Eq. (2.1), the operators having different Lorentz structures at high energy scale can turn into a mixture of them at low energy [29, 41–47]. The mixing effect can be numerically relevant when coupling strength between the dark fermion and heavy quark (particularly the top-quark) is relatively large [29, 41–47]. Here, by definition we have assumed that the above effective operators are only valid for the first generation quarks. Within this approximation, the mixing effect can be safely neglected. We will study the interaction between the dark fermion and the

third generation quarks elsewhere. Furthermore, in principle the dark fermion can couple to all the three charged leptons, and the couplings can be either universal or independent. However, inclusion of more leptons lead to diverse phenomenologies in both direct detection and collider search experiments, as well as decay of the dark fermion which is important to have a correct relic abundance. Here we simply assume that the charged lepton can only be the electron. Those assumptions are also necessary in order to have a consistent combination of the collider searches and direct detections, where only the light quarks and the electron are relevant.

### 3 Constraints at the LHC

The EFT description of collider searches can work well as long as the cut-off scales  $\Lambda_i$  are higher than the parton level center of mass energy [30], or mass of the possible mediator is much larger than the collision energy [48–50]. In consideration of that the parton level collision energy is always suppressed by the PDFs, here we simply assume that the operators defined in Eq. (2.1) are always valid. Signatures of the charged current operators are completely different from the ones of the neutral current operators. For neutral current operators, since the dark fermion and the neutrino are always represented by a missing energy at colliders, the most sensitive probes are the mono- $X$  production processes [35–38], where the  $X$  being some visible particles. For instances, the mono-photon [51–55], mono- $Z/W$  [51, 56–63] and mono-jet process [51, 64–66]. In this case the total cross sections are proportion to  $\alpha_{EM}/\Lambda^4$  or  $\alpha_s/\Lambda^4$ . In contrast, for the charged current operators defined in Eq. (2.1), there is always a visible charged lepton in dark fermion production process. As a result the total cross section is proportional to  $1/\Lambda^4$  which is roughly 2 order of magnitude enhancement. Hence it is expected that constraints on the charge current operators are much more stronger than the neutral current operators. It is clear that the most sensitive channel is mono-lepton production. We will also study details of associated productions of the dark fermion with a lepton and a photon or one jet. These processes can be used to enhance the constraints in combination, and are also useful to distinguish interaction mechanisms of the signals. Our numerical simulations are done at generator level by using the toolboxes MadGraph [67, 68] and FeynRules [69] in UFO format [70]. We will show below details of the validation of our simulations.

#### 3.1 Mono-Lepton Production

Since we have assumed that the dark fermion can only couple to the electron, the mono-lepton production turns out to be following mono-electron production at hadron collider,

$$p + p \rightarrow e^\pm + \cancel{E}_T + X, \quad (3.1)$$

where the transverse missing energy accounts for the dark fermion  $\chi(\bar{\chi})$  for the signal, and the neutrino for irreducible background. The corresponding parton-level Feynman diagrams are shown in the Fig. 1 (a) for the signal and (b) for the irreducible background. It is clear that the mono- $W^\pm$  production with leptonic subsequent decay is the major irreducible background. As a result, the irreducible background can be significantly reduced by a

kinematical cut on transverse mass of the electron and transverse missing energy. Hence it is expected that the mono-electron production is the most sensitive channel to search for the dark fermion at the LHC.

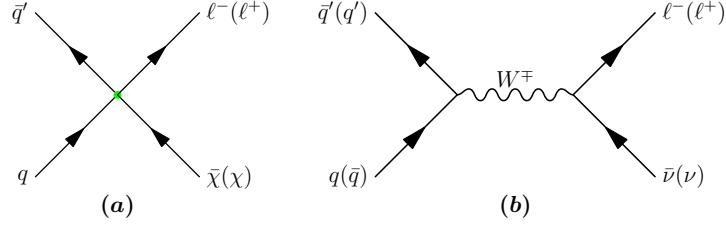


**Figure 1.** Feynman diagrams of the mono-lepton process  $pp \rightarrow \ell^\pm \cancel{E}_T + X$ : (a) is for the signal operators, (b) is for the irreducible background.

The Fig. 2 (a) and (b) show normalized polar angle ( $\theta_{e^\pm}$ ) and transverse momentum ( $p_{T,e^\pm}$ ) distributions of the electrons in the laboratory frame with center of mass energy  $\sqrt{s} = 13$  TeV, respectively. Properties of the signal events (colorful non-solid curves) are shown for parameters  $m_\chi = 0$  GeV and  $\Lambda_i = 1$  TeV, and the irreducible background is shown by black-solid curve. From the Fig. 2 (a) one can see that irrespective of the different

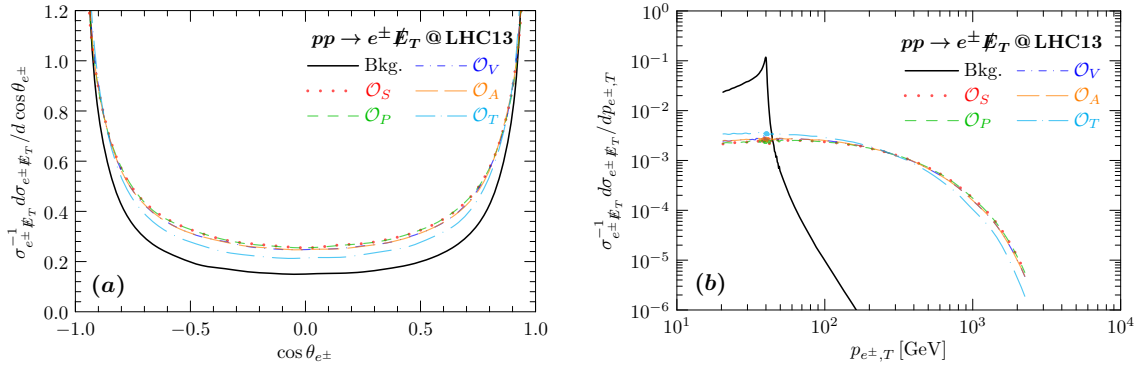


**Figure 2.** Normalized distributions of the polar angle ( $\theta_{e^\pm}$ ) (a) and transverse momentum ( $p_{e^\pm, T}$ ) (b) of the outgoing electron at generator level in the laboratory frame with center of mass energy  $\sqrt{s} = 13$  TeV. In the above panels, the signals (colorful non-solid curves) are shown for parameters  $m_\chi = 0$  GeV and  $\Lambda_i = 1$  TeV, and the background (black-solid curve) stands for the irreducible contribution from the channel  $pp \rightarrow W^\pm \rightarrow e^\pm \nu$ .

Lorentz structures of the operators in Eq. (2.1), the electrons are dominantly generated in the forward and backward regions. It is also true for the irreducible background since the  $W^\pm$  bosons are primarily emitted along the incoming partons. Hence, difference of the polar angle distribution in the central region is negligible in either enhancing signal significance or distinguishing Lorentz structures of the signal operators. In contrast, the transverse momentum is a very good observable to enhance signal significance, as shown in the Fig. 2 (b). For the irreducible background events, the electrons emerge from decays of the  $W^\pm$  bosons. As a result their transverse momentum are dominantly populated at half of the  $W^\pm$  boson mass, i.e.,  $p_{e^\pm, T} \sim m_W/2$ . Above this threshold, distribution of the  $p_{e^\pm, T}$  drops very quickly. However, transverse momentum of the signal electrons are not restricted by such a resonant decay. It is only limited by the center of mass energy  $\sqrt{s}$  and suppression

due to PDF at large energy fraction. As one can see that distribution of the  $p_{e^\pm, T}$  starts to have sizable decrease only when the  $p_{e^\pm, T}$  reaches to hundreds of GeV.

The mono-lepton production channel has been searched by both the ATALS [71, 72] and the CMS [73] collaborations for exploring heavy charged boson. The observable used to discriminate signal and background is the transverse mass of the charged lepton and the transverse missing energy, which is defined as follows,

$$m_T = \sqrt{2p_{\ell, T} \cancel{E}_T (1 - \cos \phi_{\ell\nu})}, \quad (3.2)$$

where  $\phi_{\ell\nu}$  is the azimuthal angle difference between the charged lepton and missing transverse momentum in the transverse plane. At parton level, the charged lepton and the missing momentum are always back-to-back (in the transverse plane), hence the transverse mass is simply given as 2 times of the transverse momentum of the charged lepton, *i.e.*,  $m_T = 2p_{\ell, T}$ . Fig. 3 (a) shows the normalized distributions of the parton level transverse mass at center

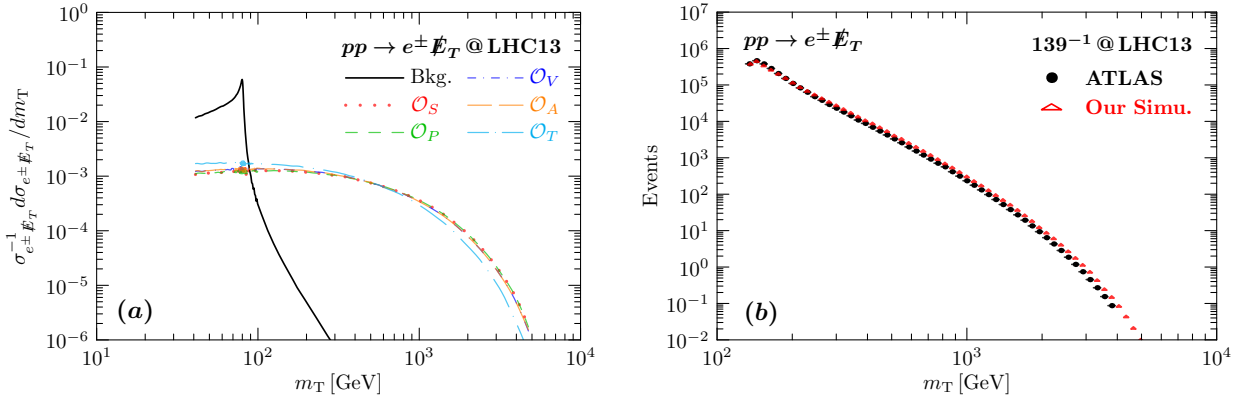


**Figure 3.** (a): Normalized distributions of the transverse mass ( $m_T$ ) of the outgoing electron and the missing transverse energy at generator level in the laboratory frame with center of mass energy  $\sqrt{s} = 13$  TeV. The signals (colorful non-solid curves) are shown for parameters  $m_\chi = 0$  GeV and  $A_i = 1$  TeV, and the background (black-solid curve) stands for the irreducible contribution from the channel  $pp \rightarrow W^\pm \rightarrow e^\pm \nu$ . (b): Validation of our simulation for the transverse mass ( $m_T$ ) distribution of the irreducible background process  $pp \rightarrow W^\pm \rightarrow e^\pm \nu$  at the LHC with center of mass energy  $\sqrt{s} = 13$  TeV and a total luminosity  $\mathcal{L} = 139 \text{ fb}^{-1}$ . The experimental results (black dots) are taken from the Ref. [71], and our results (red triangles) have been renormalized by multiplying an overall constant such that the total number of events is matched.

of mass energy  $\sqrt{s} = 13$  TeV for the signals (colorful non-solid curves) and the irreducible background (black-solid curve). One can clearly see the peak at  $m_T = m_W$  for the irreducible background. Above this resonant peak the production rate decreases dramatically, while distributions of the signals have long tails. Here we take the ATLAS' result, which has a larger luminosity  $139 \text{ fb}^{-1}$ , as a reference data set to validate our simulations. The events are selected by requiring that both the transverse missing energy  $\cancel{E}_T$  and the transverse momentum of the electrons  $p_{e^\pm, T}$  are larger than 65 GeV, and rapidity of the electrons are restricted to be  $|\eta_e| < 2.47$  and  $|\eta_e| \notin [1.37, 1.52]$  for excluding the barrel-endcap transition region. The signal region is defined by the condition  $m_T > 130$  GeV. Fig. 3 (b) shows validation of our simulation on the irreducible background process  $pp \rightarrow W^\pm \rightarrow e^\pm \nu$  in the signal region. In comparison, our result is renormalized by an universal scale factor to match



to the total number of the irreducible background events. This overall normalization factor accounts for possible detector effects. One can clearly see that our result is consistent with the ATLAS' data. Such an excellent match indicates that the approximation of an overall normalization factor works well for both the total number of events and the differential distributions.

The expected exclusion limits at the LHC13 is estimated by calculating following  $\chi^2$ ,

$$\chi^2 = \sum_i \left[ \frac{\epsilon_D \cdot N_i^S}{\sigma_i^{\text{ATLAS}}} \right]^2, \quad (3.3)$$

where  $\sigma_i^{\text{ATLAS}}$  is the experimental uncertainty of the number of events in the  $i$ -th bin of the transverse mass  $m_T$  (given by the ATLAS paper [71]),  $N_i^S$  is the number of signal events in the  $i$ -th bin, and  $\epsilon_D$  is the detector efficiency as we have explained above. The Fig. 4 shows the expected exclusion limits at 95% C.L. in the  $m_\chi - \Lambda$  plane. One can see that the

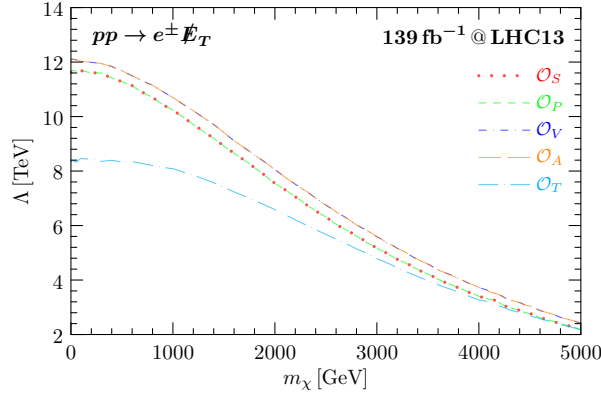


**Figure 4.** Expected exclusion limits at 95% C.L. by using the associated production of an electron with transverse missing energy,  $pp \rightarrow e^\pm \cancel{E}_T$ , at the LHC with center of mass energy  $\sqrt{s} = 13$  TeV and a total luminosity  $\mathcal{L} = 139 \text{ fb}^{-1}$ .

mono-electron process is most sensitive to the (axial)-vector operators. For a massless dark fermion, the strongest lower limit can reach to about 12 TeV. Constraints on the (pseudo)-scalar operators are slightly weaker, and the lower limit is about 11.6 TeV in case of that  $m_\chi \sim 0$ . The weakest bound is for the tensor operator, and the lower limit is about 8.4 TeV for an ultra-light dark fermion. However, the differences become smaller and smaller with increasing mass of the dark fermion. For a heavy dark fermion with mass about 5 TeV, the lower bound on the energy scale is roughly 2 TeV for all the operators.

### 3.2 Associated Production of Lepton with Photon

Apart from the mono- $\ell$  signal, the effective operators defined in Eq. (2.1) can also induce following associated production of transverse missing energy with a lepton and a photon,

$$p + p \rightarrow e^\pm + \gamma + \cancel{E}_T + X. \quad (3.4)$$

For the signals, the photon can emerge from either initial state or final state radiations, as shown in the Fig. 5 (a) and (b) for the corresponding parton level Feynman diagrams,



respectively. For the background, besides the case of that the photons are emitted from either incoming partons or outgoing leptons (as shown in the Fig. 5 (c) and (d)), there is an additional contribution from the  $W^\pm$  radiation, as shown in the Fig. 5 (e). Compared to the mono- $\ell$  production, both the signal and background are suppressed by a factor of  $\alpha_{\text{EM}}$ . As a result, signal significance is also reduced by a factor of about  $\sqrt{\alpha_{\text{EM}}}$ , roughly one order of magnitude reduction. Since the cross section is proportional to  $\Lambda^{-4}$ , the lower bound of the energy scale can be reduced roughly by a factor of 2. However, since one has more visible particles in the final state, it is possible to extract further information about the Lorentz structures of the interaction vertex. Hence, it is worthy to study this channel in details.

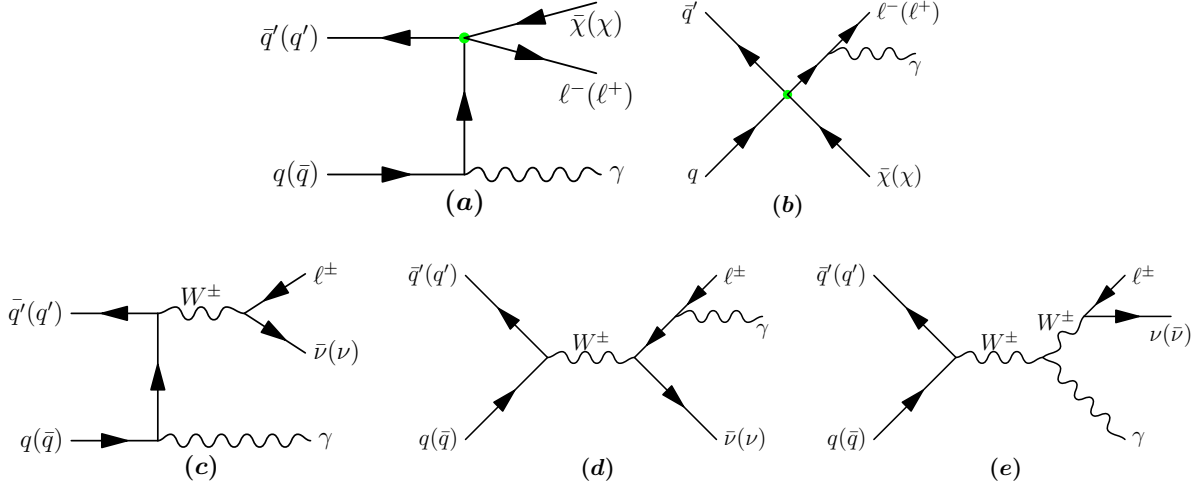


**Figure 5.** Feynman diagrams of the associated production of a lepton and a photon with missing energy: (a) and (b) are for the signal operators, (c), (d) and (e) are for the irreducible background.

The Fig. 6 (a) and (b) show normalized polar angle distributions of the electron ( $\theta_{e^\pm}$ ) and of the photon ( $\theta_\gamma$ ) in the laboratory frame with center of mass energy  $\sqrt{s} = 13$  TeV, respectively. Properties of the signal events (colorful non-solid curves) are shown for parameters  $m_\chi = 0$  GeV and  $\Lambda_i = 1$  TeV, and the irreducible background is shown by black-solid curve. From the Fig. 6 (a) one can see that polar angle distributions of the electron is much similar to the case of the mono-electron production, for both the signal and the irreducible background: most of the electrons are distributed in the forward and backward regions. Since the photons are from initial state and final state radiations. most of the photons are also distributed in the forward and backward regions, as one can see from the Fig. 6 (b). The normalized distributions of the missing transverse energy ( $\cancel{E}_T$ ) and transverse momentum of the photon ( $p_{\gamma,T}$ ) are shown in the Fig. 6 (c) and (d), respectively. For the irreducible background, since the missing energy comes from  $W^\pm$  boson decay, the missing transverse energy  $\cancel{E}_T$  has a sharp peak at  $\cancel{E}_T \sim m_W/2$ . In contrast, there is no such a resonant peak in distribution of the transverse momentum of the photon  $p_{\gamma,T}$ , as shown in the Fig. 6 (d). The Fig. 6 (e) shows the normalized distributions of the transverse mass of the electron momentum and missing momentum (as defined in Eq. (3.2)). Since appearance of an additional photon, most of the events are distributed in the small  $m_T$  region. However,

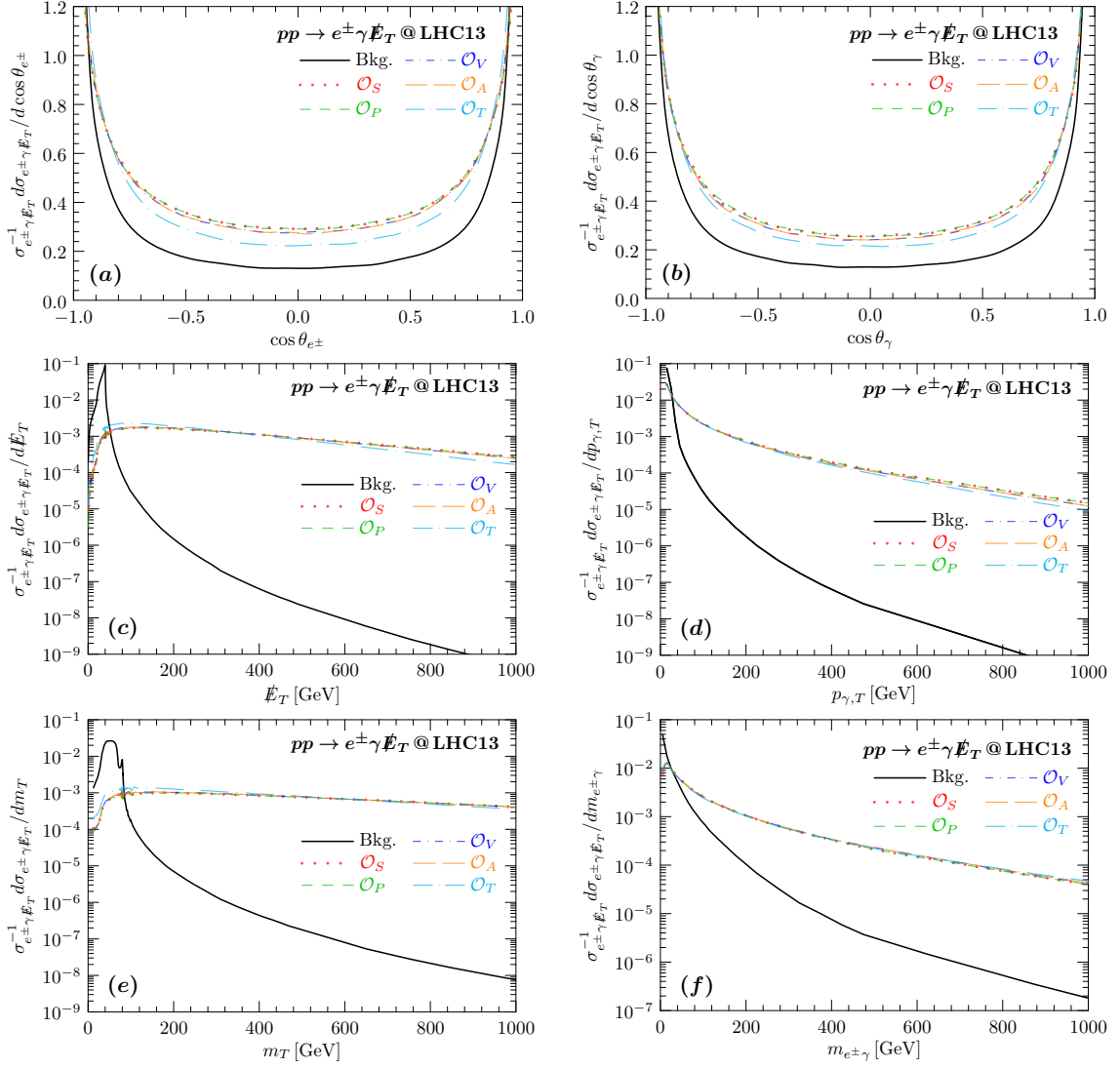


**Figure 6.** Normalized distributions of the polar angles of the outgoing electron ( $\theta_{e^\pm}$ ) (a) and photon ( $\theta_\gamma$ ) (b), transverse momentum of the missing energy ( $\cancel{E}_T$ ) (c) and the photon ( $p_{\gamma,T}$ ) (d), transverse mass of the electron and the missing energy ( $m_T$ ) (e) and invariant mass of the outgoing electron and photon ( $m_{e^\pm\gamma}$ ) (f) at the generator level in the laboratory frame with center of mass energy  $\sqrt{s} = 13$  TeV. In the above panels, the signals (colorful non-solid curves) are shown for parameters  $m_\chi = 0$  GeV and  $\Lambda_i = 1$  TeV, and the background (black-solid curve) stands for the irreducible contribution from the channel  $pp \rightarrow e^\pm\gamma\nu$ .

as expected, one can still see a peak at  $m_T \sim m_W$ . The Fig. 6 (f) shows the normalized distributions of the invariant mass of the outgoing electron and photon ( $m_{e^\pm\gamma}$ ). Both the signals and the irreducible background decrease with increasing  $m_{e^\pm\gamma}$ , but the background drops more quickly than the signals. This is a general property of the signals for all the four observables: transverse missing energy  $\cancel{E}_T$ , transverse momentum of the photon  $p_{\gamma,T}$ , transverse mass  $m_T$  and invariant mass  $m_{e^\pm\gamma}$ . Hence all of them can be used to enhance signal significances.

The CMS collaboration searched for supersymmetry in events containing a photon, a charged lepton and large missing transverse momentum [74] at the LHC with center of mass energy  $\sqrt{s} = 13$  TeV and a total luminosity of  $35.9 \text{ fb}^{-1}$ . Here we take the CMS' result

as a reference data set to validate our simulation. The events are selected by requiring that the transverse momentum of the photon  $p_{\gamma,T}$  is larger than 35 GeV, and its rapidity is restricted in a small range  $|\eta_\gamma| < 1.44$ ; the transverse momentum of the electron  $p_{e,T}$  is larger than 25 GeV, and its rapidity is restricted to be  $|\eta_e| < 2.5$  and  $|\eta_e| \notin [1.44, 1.56]$  for excluding the barrel-endcap transition region. The photon is also required to be separated from the electron by a relatively large distance,  $\Delta R_{e\pm\gamma} > 0.5$ , to suppress contributions from the final state radiation. Furthermore, the invariant mass  $m_{e\pm\gamma}$  is required to be at least 10 GeV greater than the  $Z$  boson mass to reduce the contribution of  $Z \rightarrow e^+e^-$  in case of that one of the electrons is misidentified as a photon. The signal region is defined by the conditions  $\cancel{E}_T > 120$  GeV and  $m_T > 100$  GeV. Since we did not consider parton shower effect, we used in our simulation a relatively smaller but reasonable cut on the transverse mass,  $m_T > 80$  GeV to avoid huge reduction of the background. Fig. 7 (a) and (b) show validations of our simulations on the irreducible background process  $pp \rightarrow e^\pm\gamma\nu$  for the observables  $\cancel{E}_T$  and  $p_{\gamma,T}$ . Our result is renormalized by an universal scale factor to account

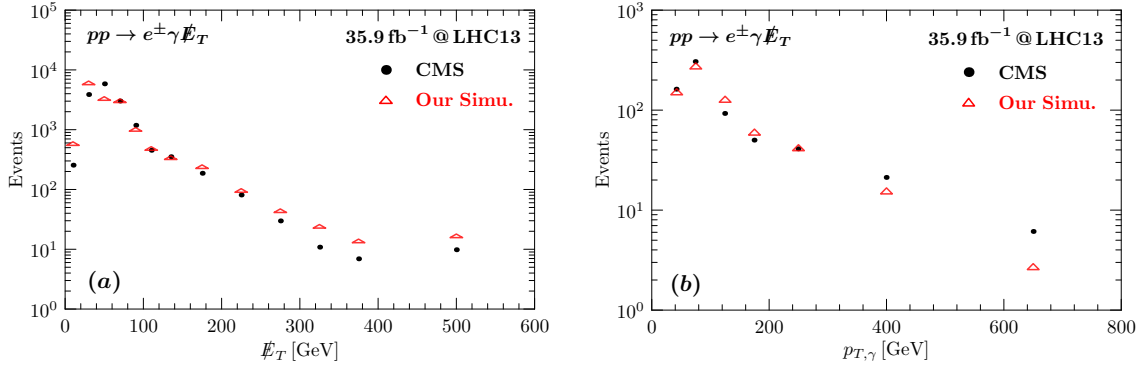


**Figure 7.** Validation of our simulations for the transverse missing energy ( $\cancel{E}_T$ ) and transverse momentum of the photon  $p_{\gamma,T}$  distributions of the irreducible background process  $pp \rightarrow e^\pm\gamma\nu$  at the LHC with center of mass energy  $\sqrt{s} = 13$  TeV and a total luminosity  $\mathcal{L} = 35.9 \text{ fb}^{-1}$ . The experimental results (black dots) are taken from the Ref. [74], and our results (red triangles) have been renormalized by multiplying an overall constant such that the total number of events is matched.

for the strong reduction efficiency of cut  $m_T > 80$  GeV and possible detector effects. One can see that for both these two observables the CMS' results can be roughly reproduced. There is a relatively sizable deficiency in the soft region of the transverse missing energy. But it can not affect our estimation of the exclusion limit because of the strong cut  $\cancel{E}_T > 120$  GeV. Hence the approximation of an overall normalization factor works well for both the total number of events and the differential distributions.

The CMS collaboration used a complex procedure to estimate the exclusion limit. In our case, in consideration of that we have different interested parameter space, the expected exclusion limits are estimated by calculating following  $\chi^2$ ,

$$\chi^2 = \sum_{\mathcal{O}} \sum_{\mathcal{O}_i} \frac{[\epsilon_D \cdot N_{\mathcal{O}_i}^S]^2}{\sqrt{\epsilon_D \cdot (\epsilon_R \cdot N_{\mathcal{O}_i}^B + N_{\mathcal{O}_i}^S)}}, \quad (3.5)$$

where  $\mathcal{O} = \cancel{E}_T, p_{\gamma,T}, m_T$  and  $m_{e\pm\gamma}$  are the four observables used to enhance the signal

significances,  $N_{\mathcal{O}_i}^S$  and  $N_{\mathcal{O}_i}^B$  are number of events of the signals and the irreducible background in the  $\mathcal{O}_i$ -th bin of the observable  $\mathcal{O}$ ,  $\epsilon_D$  is an universal normalization factor to account for the detector efficiency as we have explained above, and the scale factor  $\epsilon_R$  is used to account for contributions of the reducible background. The Fig. 8 shows the expected exclusion limits at 95% C.L. in the  $m_\chi - \Lambda$  plane. As expected (similar to the mono-electron production),

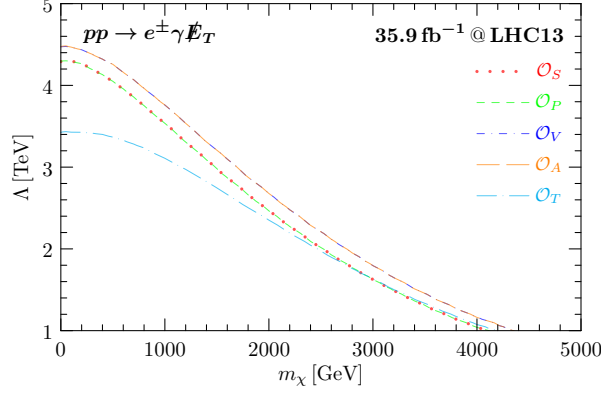


**Figure 8.** Expected exclusion limits at 95% C.L. by using the associated production of an electron and a photon with transverse missing energy,  $pp \rightarrow e^\pm \gamma \cancel{E}_T$ , at the LHC with center of mass energy  $\sqrt{s} = 13$  TeV and a total luminosity  $\mathcal{L} = 35.9 \text{ fb}^{-1}$ .

constraints on the (axial-)vector operators are the strongest, and constraints on the (pseudo-)scalar operators are slightly weaker. The weakest bound is given for the tensor operator. For a massless dark fermion, the lower bounds on the energy scales of the (axial-)vector, (pseudo-)scalar and tensor operators, can reach to about 4.43 TeV, 4.25 TeV and 3.41 TeV, respectively. However, the differences diminish gradually for a heavy dark fermion. For  $\Lambda_i = 1$  TeV, a heavy dark fermion with mass up to about 4 TeV can be excluded for all kinds of the operators.

### 3.3 Associated Production of Lepton with Jet

Much similar to the associated production of missing energy with a lepton and a photon through initial and final state radiations, the effective operators defined in Eq. (2.1) can also induce following associated production of missing energy with a lepton and one jet,

$$p + p \rightarrow e^\pm + j + \cancel{E}_T + X. \quad (3.6)$$

However, in this case the additional jet in signal process can not only be generated from emission of the incoming partons (as shown in the Fig. 9 (a) and (b) for the parton level Feynman diagrams), but also can be generate via a  $s$ -channel exchange of an off-shell quark, as shown in the Fig. 9 (c). Furthermore, the gluons of the incoming hadrons can give nontrivial contributions. This is also true for the irreducible background, as shown in the Fig. 9 (d), (e) and (f). Compared to the mono-electron production channel, total cross sections of both the signal and background of this associated production are suppressed by a factor of  $\alpha_s$ . As a result, signal significance is reduced by a factor of about  $\sqrt{\alpha_s}$ , roughly one-third of reduction. For the energy scale  $\Lambda_i$ , the suppression factor is about 3/4. Hence it is expected to have a comparable exclusion limit to the mono-electron production

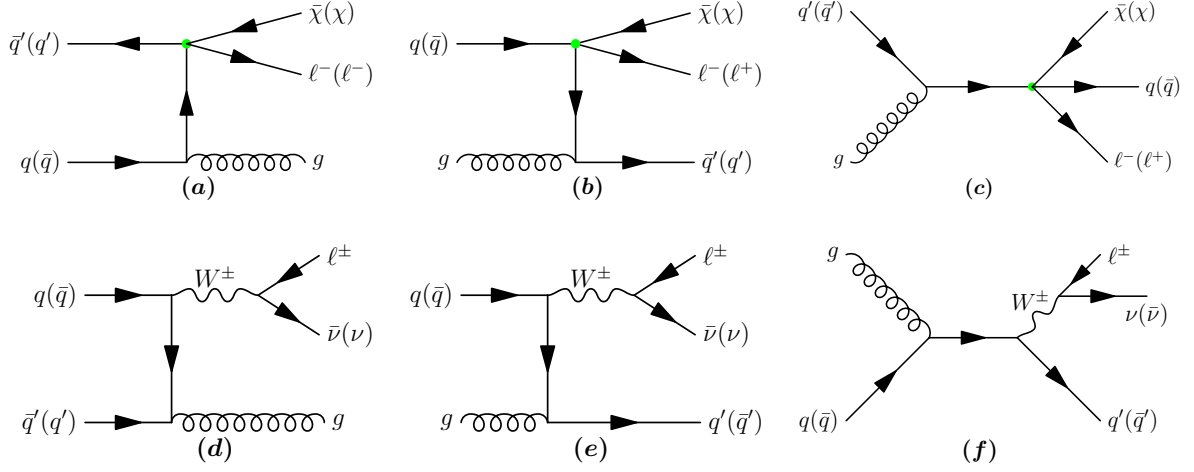


**Figure 9.** Feynman diagrams of the associated production of a lepton and one jet with missing energy: (a), (b) and (c) are for the signal operators, (d), (e) and (f) are for the irreducible background.

channel. Again, because one more visible particle in the final state, more information about the Lorentz structures of the interaction vertex can be obtained by further analysis of the angular distributions and correlations of the final state particles. Furthermore, since initial state configuration is completely different from the one of the associated production of missing energy with a lepton and a photon, and also different generation channels, it is expected that sensitivities to the different operators are also different. Hence, it is worthy to study this production process in details.

The Fig. 10 (a) and (b) show normalized polar angle distributions of the electron ( $\theta_{e^\pm}$ ) and of the jet ( $\theta_j$ ) in the laboratory frame with center of mass energy  $\sqrt{s} = 13 \text{ TeV}$ , respectively. Distributions of the signal events (colorful non-solid curves) are shown for parameters  $m_\chi = 0 \text{ GeV}$  and  $\Lambda_i = 1 \text{ TeV}$ , and the irreducible background is shown by the black-solid curve. One can clearly see that polar angle distributions of the electron and jet are dominant at the forward and backward regions. This is simply a result of that the major production mechanism is the initial state radiation (of  $W^\pm$  boson and jet). The normalized distributions of the missing transverse energy ( $\cancel{E}_T$ ) and transverse momentum of the jet ( $p_{\gamma,T}$ ) are shown in Fig. 10 (c) and (d), respectively. Once more, since the transverse missing energy of the irreducible background comes from the neutrino of the  $W^\pm$  boson decay, its distribution has a peak at  $\cancel{E}_T \sim m_W/2$ . However, the peak is not as sharp as the ones of the mono-electron production and the associated production of missing energy with an electron and a photon. This is because that when the incoming parton is a gluon, the radiated parton can be harder than the photon from a similar initial state radiation. This can be seen by comparing the Fig. 10 (d) and Fig. 6 (d): transverse momentum of the photon drops more quickly. The Fig. 10 (e) shows the normalized distribution of the transverse mass of the electron momentum and missing momentum (as defined in Eq. (3.2)). Since the emitted jet is completely isolated from the  $W^\pm$  boson decay, the bound on the transverse mass  $m_T$  is as strong as the mono-electron production channel (stronger than the associated production of missing energy with  $e^\pm$  and  $\gamma$ , as shown in the Fig. 6 (e)). One can see a very sharp peak at  $m_T \sim m_W$ . The Fig. 10 (f) shows the normalized distribution

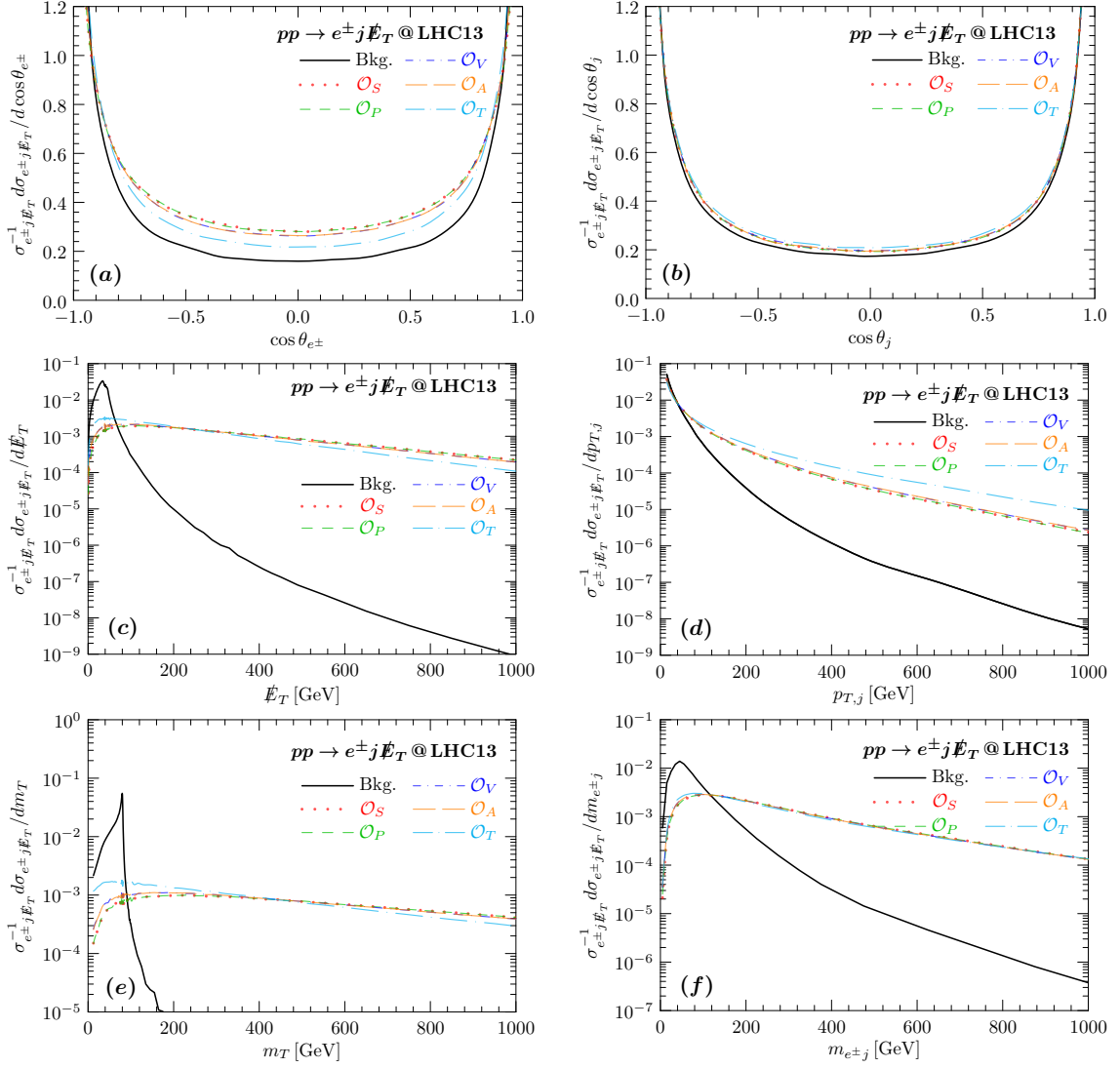


**Figure 10.** Normalized distributions of the polar angles of the outgoing electron ( $\theta_{e^\pm}$ ) (a) and the jet ( $\theta_j$ ) (b), transverse momentum of the missing energy ( $\cancel{E}_T$ ) (c) and the jet ( $p_{T,j}$ ) (d), transverse mass of the electron and the missing energy ( $m_T$ ) (e) and invariant mass of the outgoing electron and jet ( $m_{e^\pm j}$ ) (f) at the generator level in the laboratory frame with center of mass energy  $\sqrt{s} = 13$  TeV. In the above panels, the signals (colorful non-solid curves) are shown for parameters  $m_\chi = 0$  GeV and  $\Lambda_i = 1$  TeV, and the background (black-solid curve) stands for the irreducible contribution from the channel  $pp \rightarrow e^\pm j \nu$ .

of the invariant mass ( $m_{e^\pm j}$ ) of the outgoing electron and jet. The background events are dominantly distributed in the soft region, while the signal contributions are still sizable in the large invariant mass region. Similarly, the property of that, the background events are populated in the soft region while the signal events are much harder, is true for all the four observables: transverse missing energy  $\cancel{E}_T$ , transverse momentum of the photon  $p_{j,T}$ , transverse mass  $m_T$  and invariant mass  $m_{e^\pm j}$ . In our estimation of the exclusion limits, all of them will be used to enhance the signal significances.

The ATLAS collaboration searched for quantum black hole production in the one lepton and a jet final states at the LHC with center of mass energy  $\sqrt{s} = 13$  TeV and a luminosity of  $140 \text{ fb}^{-1}$  [75]. Here we take the ATLAS' result as the reference data set to validate

our simulation. The events are selected by requiring that transverse momentum of the jet  $p_{j,T}$  is larger than 130 GeV, and its rapidity is restricted in the range  $|\eta_j| < 2.8$ ; the transverse momentum of the electron  $p_{e,T}$  is required to be larger than 130 GeV, and its rapidity is restricted to be  $|\eta_e| < 2.5$  and  $|\eta_e| \notin [1.37, 1.52]$  for excluding the barrel-endcap transition region. The jet is further required to be separated from the electron by a distance  $\Delta R_{e\pm\gamma} > 0.4$ . Furthermore, the invariant mass  $m_{e\pm j}$  is required to be at least 10 GeV greater than the  $Z$  boson mass to reduce the contribution of  $Z \rightarrow e^+e^-$  in case of that one of the electrons is misidentified as a jet. The signal region is defined by the condition  $m_{e\pm j} > 1$  TeV. Fig. 11 (a) shows validation of our simulation on the irreducible background

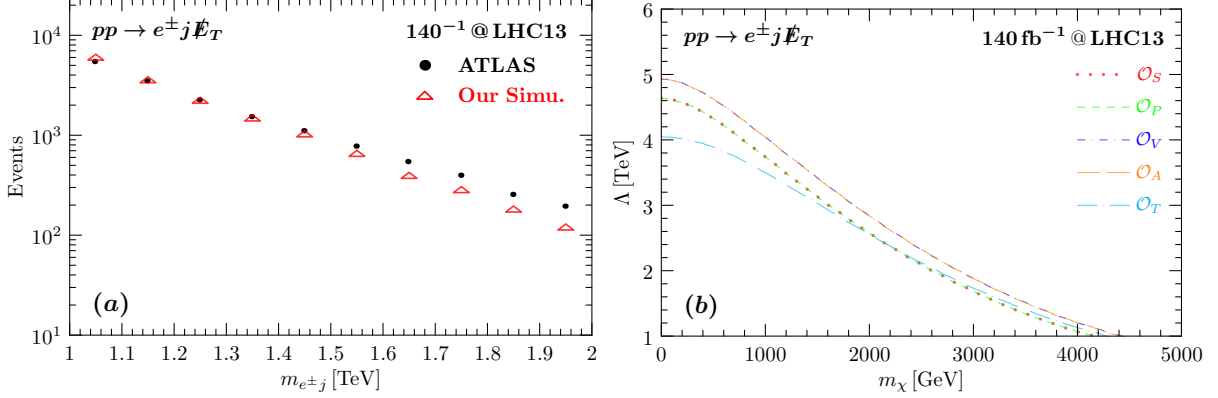


**Figure 11.** (a): Validation of our simulation for the invariant mass ( $m_{e\pm j}$ ) distribution of the outgoing electron and jet of the irreducible background process  $pp \rightarrow e^{\pm} j \cancel{E}_T$  at the LHC with center of mass energy  $\sqrt{s} = 13$  TeV and a total luminosity  $\mathcal{L} = 140 \text{ fb}^{-1}$ . The experimental results (black dots) are taken from the Ref. [75], and our results (red triangles) have been renormalized by multiplying an overall constant such that the total number of events is matched. (b): Expected exclusion limits at 95% C.L. by using the validated simulation of the process  $pp \rightarrow e^{\pm} j \cancel{E}_T$  at the LHC with center of mass energy  $\sqrt{s} = 13$  TeV and a total luminosity  $\mathcal{L} = 35.9 \text{ fb}^{-1}$ .

process  $pp \rightarrow e^{\pm} j \nu$  for the invariant mass distribution of the electron and jet,  $m_{e\pm j}$ . Our result is renormalized by an universal scale factor which is extracted by matching the total event number of our simulation to the one given by the ATLAS paper. Again, this factor accounts for the possible detector effects. One can see that our simulation result is consistent with the ATLAS' data. Hence the approximation of an overall normalization factor works well for both the total number of events and the differential distributions.

For estimation of the exclusion limit, since we are interested in different parameter space, instead of requiring  $m_{e\pm j} > 1$  TeV, we define the signal region by the condition  $m_T > 100$  GeV. As we can see from the Fig. 10 (e), the transverse mass is a powerful observable to reduce the background. Within this signal region, the expected exclusion limits are estimated by calculating  $\chi^2$  function defined in Eq. (3.5). The Fig. 11 (b) shows the 95% expected exclusion limits in the  $m_{\chi} - \Lambda$  plane for our signal operators. Similar to the mono-electron and the associated  $e^{\pm}\gamma$  production, the strongest bounds are given for the (axial)-vector operators. The different thing is that constraint on the tensor operator is comparable to, or even stronger than the ones on the (pseudo)-scalar operators. For a massless dark fermion, the lower bounds on the energy scales of the (axial)-vector, (pseudo)-scalar and tensor operators, can reach to about 4.4 TeV, 4.0 TeV and 4.0 TeV, respectively.



It is clear that the differences diminish gradually for a heavy dark fermion. For  $\Lambda_i = 1$  TeV, a heavy dark fermion with mass up to about 4 TeV can be excluded for all the kinds of operators.

### 3.4 Constraints at Future Hadron Colliders

As a general property that the signal cross sections of the four fermion contact operators grows quickly with respect to the center-of-mass energy, and meanwhile the one of the corresponding background decreases, it is in order to study future sensitivities at upgrades of the LHC[76]. Furthermore, much larger total luminosity than the current LHC will be accumulated at the upgrades. Hence upgrades of the LHC have great advantages for probing the signals. The Tab. 1 lists the configurations studied in this paper: the LHC14 with center of mass energy  $\sqrt{s} = 14$  TeV and a total luminosity  $\mathcal{L} = 3 \text{ ab}^{-1}$ , and the LHC25 with center of mass energy  $\sqrt{s} = 25$  TeV and a total luminosity  $\mathcal{L} = 20 \text{ ab}^{-1}$ . The corresponding kinematical cuts for the three production processes are also listed in the Tab. 1.

Process	14 TeV, $3 \text{ ab}^{-1}$	25 TeV, $20 \text{ ab}^{-1}$
$pp \rightarrow e^\pm \cancel{E}_T$	$p_{T,e} \geq 65 \text{ GeV},  \eta_e  \leq 2.5$	$p_{T,e} \geq 150 \text{ GeV},  \eta_e  \leq 2.5$
	$\cancel{E}_T \geq 65 \text{ GeV}$	$\cancel{E}_T \geq 150 \text{ GeV}$
$pp \rightarrow e^\pm \gamma \cancel{E}_T$	$p_{T,e} \geq 25 \text{ GeV},  \eta_e  \leq 2.5$	$p_{T,e} \geq 50 \text{ GeV},  \eta_e  \leq 2.5$
	$p_{T,\gamma} \geq 35 \text{ GeV},  \eta_\gamma  \leq 1.44$	$p_{T,\gamma} \geq 70 \text{ GeV},  \eta_\gamma  \leq 1.44$
	$\Delta R_{e,\gamma} \geq 0.8$	$\Delta R_{e,\gamma} \geq 1$
	$ m(e, \gamma) - m_Z  > 10 \text{ GeV}$	$ m(e, \gamma) - m_Z  > 10 \text{ GeV}$
	$\cancel{E}_T \geq 120 \text{ GeV}, m_T \geq 80 \text{ GeV}$	$\cancel{E}_T \geq 200 \text{ GeV}, m_T \geq 80 \text{ GeV}$
$pp \rightarrow e^\pm j \cancel{E}_T$	$p_{T,e} \geq 130 \text{ GeV},  \eta_e  \leq 2.5$	$p_{T,e} \geq 250 \text{ GeV},  \eta_e  \leq 2.5$
	$p_{T,j} \geq 130 \text{ GeV},  \eta_j  \leq 2.8$	$p_{T,j} \geq 250 \text{ GeV},  \eta_j  \leq 2.8$
	$\Delta R_{e,j} \geq 0.4$	$\Delta R_{e,j} \geq 0.4$
	$ m(e, j) - m_Z  > 10 \text{ GeV}$	$ m(e, j) - m_Z  > 10 \text{ GeV}$
	$m_T \geq 100 \text{ GeV}$	$m_T \geq 200 \text{ GeV}$

**Table 1.** Configurations of the upgrades of the LHC and the corresponding kinematical cuts at parton level.

The Fig. 12 shows the expected exclusion limits at 95% C.L. at the LHC14 (top panels) and  $\sqrt{s} = 25$  TeV (bottom panels). From the left to right, the Fig. 12 (a) and (b) stands for the mono-electron production channel, the Fig. 12 (c) and (d) show the results for the associated production of an electron and a photon with missing energy, and the results for the associated production of an electron and one jet with missing energy are shown in the Fig. 12 (e) and (f). One can clearly see that the mono-electron production is still the most sensitive process to the four fermion contact operators. The  $e^\pm \gamma$  associated production with

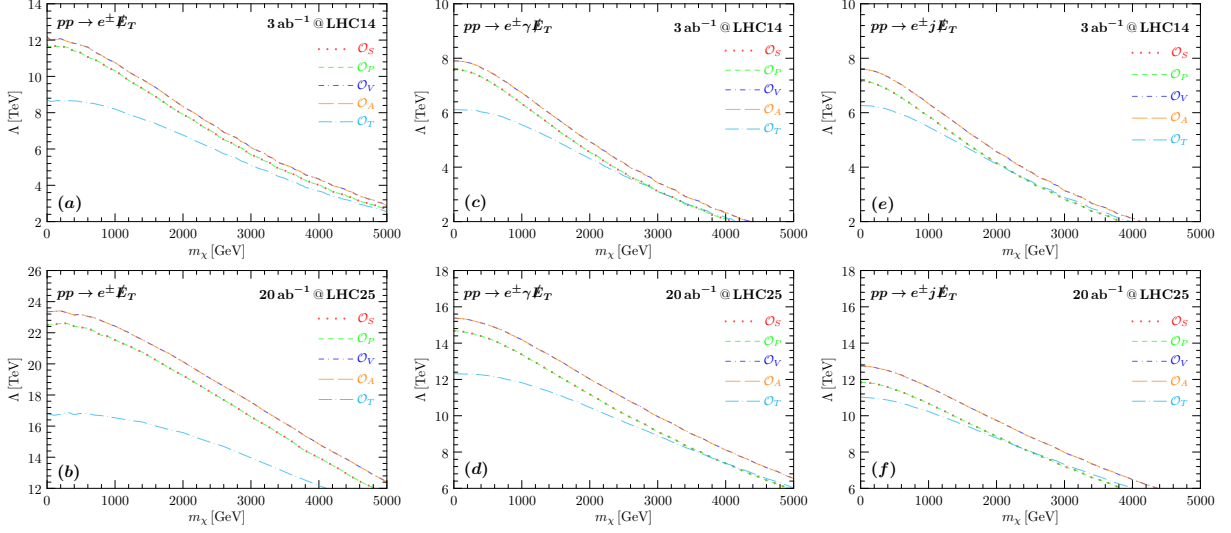


**Figure 12.** Expected exclusion limits at 95% C.L. at the LHC with center of mass energy  $\sqrt{s} = 14$  TeV and a total luminosity  $\mathcal{L} = 3 \text{ ab}^{-1}$  (top panels), and  $\sqrt{s} = 25$  TeV and a total luminosity  $\mathcal{L} = 20 \text{ ab}^{-1}$  (bottom panels): (a) and (b) stands for the mono-electron production channel, (c) and (d) stands for the associated production of an electron and a photon with missing energy, (e) and (f) stands for the associated production of an electron and one jet with missing energy.

missing energy gives much weaker constraints, but slightly stronger than the ones given by the  $e^\pm j$  associated production with missing energy. Furthermore, the strongest constraints are given for the (axial-)vector operators, the (pseudo-)scalar operators have slightly weaker bounds, and the weakest one is given for the tensor operator. This property is true for all the three channels. For the two associated production channels, the LHC14 can significantly enhance the constraints by a factor of about  $1.5 \sim 1.7$ . However, for the mono-electron channel, the enhancement is negligible. This may be due to that we have used the same bins (extracted from the ATLAS paper) for both the LHC13 and LHC14, and some phase space which has larger signal significance lies outside of those bins. In contrast, we can see a factor of about 2 enhancement at the LHC25. In next section, we will discuss how the above improvements interplay with the direction detection experiments.

## 4 Induced $\beta$ Decay

The effective operators defined in Eq. (2.1) can also lead to nontrivial signals in direct detection experiments [16, 17]. While signal of the four fermion operator involving a dark fermion and a neutrino is represented by recoil of the nucleus, the four fermion operator involving a dark fermion and a charged lepton can initiate induced  $\beta$ -decay. In case of that mass of the dark fermion  $m_\chi$  is larger than the threshold,  $m_{\text{th}}^{\beta^\mp} \equiv M_{A,Z\pm 1}^{(*)} + m_e - M_{A,Z}$  (with  $M_{A,Z}$  being mass of the nucleus of the isotope  ${}^A_Z\text{X}$ ), of the following two nuclear transition,

$$\chi(\vec{p}_\chi = m_\chi \vec{v}_\chi) + {}^A_Z\text{X}(\vec{p}_i = \vec{0}) \rightarrow {}^A_{Z\pm 1}\text{X}(\vec{p}_f) + e^\mp(\vec{p}_e), \quad (4.1)$$

then induced  $\beta$  transition can be triggered. And the corresponding two absorption channels at nucleon levels are given as follows,

$$\begin{aligned}\beta^- : \quad \chi + n &\rightarrow p + e^-, \\ \beta^+ : \quad \bar{\chi} + p &\rightarrow n + e^+.\end{aligned}\tag{4.2}$$

If mass of the dark fermion is larger than the typical binding energy of the nucleus (10 MeV), the outgoing proton/neutron after absorption can gain enough energy to escape the nucleus, and hence new signals can appear [77]. Here we restricted ourselves to the case of that  $m_\chi < 10$  MeV. In this case, the nuclei will be seen by the dark fermion as a whole target, and the scattering rate is given as [17],

$$R = \frac{\rho_\chi}{2m_\chi} \sum_j N_{T,j} n_j \langle \sigma v \rangle_j, \tag{4.3}$$

where  $\rho_\chi \approx 0.3 \text{ GeV} \cdot \text{cm}^{-3}$  is the local dark matter density;  $j$  stands for the set of target isotopes, and  $N_{T,j}$  is the number of targets of a given isotope; the factor  $n_j$  accounts for the total number of the nucleons of the targets, and  $n_j = A_j - Z_j$  and  $Z_j$  for  $\beta^-$  and  $\beta^+$  transitions, respectively;  $\langle \sigma v \rangle_j$  is the averaged cross section of the scattering off the target isotope  $j$ . In the center of mass frame, the differential cross section is given as,

$$\frac{d\sigma}{d\Omega} = \frac{1}{64\pi^2 E_{\text{cm}}^2} \frac{|\vec{p}_e|}{|\vec{p}_\chi|} \sum_{\text{transitions}} |\overline{\mathcal{M}_N}|^2, \tag{4.4}$$

where  $\mathcal{M}_N$  is the scattering amplitude,  $d\Omega = d\cos\theta d\phi$  is the solid angle element of the emitted electron/positron,  $E_{\text{cm}}$  is the center of mass energy,  $\vec{p}_e$  and  $\vec{p}_\chi = m_\chi v_\chi$  are the momentum of the electron/positron and the dark fermion, respectively. In addition, all possible nuclear spin states have been summed over. In our case,  $m_e, m_\chi, m_{\text{th},j}^\beta \ll M_{A_j, Z_j}$ , the center of mass frame is essentially the Lab. frame, and the center of mass energy can be excellently approximated as  $E_{\text{cm}} \approx M_{A_j, Z_j}$ , while momentum of the electron is approximately given as  $|\vec{p}_e|_j^2 = (m_{\text{th},j}^\beta - m_\chi)(m_{\text{th},j}^\beta - m_\chi - 2m_e)$ . Furthermore, in most cases, angular dependence of the scattering amplitude is trivial, particularly in the limit of vanishing momentum transfer. Hence the solid angle can be simply integrated out. Within this approximation, the thermally averaged cross section is given as,

$$\langle \sigma v \rangle_j = \frac{|\vec{p}_e|_j}{16\pi m_\chi M_{A_j, Z_j}^2} |\overline{\mathcal{M}_{N_j}}|^2. \tag{4.5}$$

Then, the total transition rate can be written as,

$$R = \frac{\rho_\chi}{2m_\chi} \sum_j \frac{N_{T,j} n_j |\vec{p}_e|_j}{16\pi m_\chi M_{A_j, Z_j}^2} |\overline{\mathcal{M}_{N_j}}|^2. \tag{4.6}$$

#### 4.1 Induced $\beta^-$ Decay

The transition amplitude  $\mathcal{M}_{N_j}$  can be simplified by employing the corresponding matrix element of the induced beta decay of the nuclei by the SM neutrino. In term of the scattering amplitude  $\mathcal{M}$  of the induced  $\beta^-$  transitions for single nucleon, *i.e.*, the process  $\chi + n \rightarrow p + e^-$ , the nuclei level amplitude  $\mathcal{M}_{N_j}$  can be factorized as [77, 78],

$$\mathcal{M}_N = \sqrt{\mathcal{F}(Z+1, E_e)} \mathcal{M}, \quad (4.7)$$

where the factor  $\mathcal{F}(Z+1, E_e)$  stands for the usual Fermi function, which accounts for Coloumb interactions of the charged outgoing nucleon and electron, and is given by,

$$\mathcal{F}(Z, E_e) = 2(1+S) \frac{|\Gamma(S+i\eta)|^2}{\Gamma(1+S)^2} (2r_N |\vec{p}_e|)^{2S-2} e^{\pi\eta}, \quad (4.8)$$

where  $\eta = \alpha Z \beta_e^{-1}$  with  $\beta_e^{-1}$  being velocity of the electron, and  $S = \sqrt{1 - \alpha^2 Z^2}$ , the nuclear radius is given by  $r_N = 1.2 \text{ fm } A^{1/3}$ . For energetic electron,  $E_e \gg m_e$ , the Fermi function increases with increasing proton number  $Z$ . It is worthy to note that momentum of the nucleon ( $p/n$ ) of the nucleon level process,  $\chi + n \rightarrow p + e^-$ , should be normalized to nuclei mass, *i.e.*,  $p_{\text{proton/neutron}}^2 = M_{A_j, Z_j}^2$ . The total event rate for the induced  $\beta^-$  decay can be simply rewritten as,

$$R = \frac{\rho_\chi}{2m_\chi} \sum_j \frac{N_{T,j} n_j |\vec{p}_e|_j}{16\pi m_\chi M_{A_j, Z_j}^2} \mathcal{F}(Z+1, E_e) |\mathcal{M}|^2. \quad (4.9)$$

Calculation of the nucleon level transition amplitude  $\mathcal{M}$  is not straightforward from our definitions of the effective operators given in Eq. (2.1). The matrix elements at quark level have to be matched to the ones involving nucleon [47, 79]. The operators given in Eq. (2.1) is generally parameterized for all 5 possible Lorentz structures. For neutral current, all four fermion contact operators have non-vanishing low energy counterpart [47, 79]. However, it is not true for the charged current. For the usual beta decay, it was known that the scalar and tensor couplings can not be distinguished from the vector and axial-vector couplings by the shape of the electron spectrum [40]. Additional contribution beyond the standard  $V - A$  coupling form of the electroweak interaction can only be measured by the Fierz interference [80–82]. However, so far there is no any evidence of non-vanishing contribution from the scalar, pseudo-scalar and tensor operators [83], and the Fierz interference is strongly constrained [84–86]. Even through a combined analysis suggests a finite value of the Fierz interference (2.86 $\sigma$  deviation from the SM [84]), we still use the conservative assumption of that only vector and axial-vector operators of the quark fields can induce non-vanishing nucleon matrix elements.

According to the induced beta decay for the SM neutrino, matrix elements of the vector and axial-vector operator at quark level can be parameterized at nucleon level as follows [77] (the scalar and tensor components have been automatically removed in consideration

of that the form factors vanishes since isospin invariance of the strong interaction),

$$\langle f | \bar{Q} T^a \gamma^\mu Q | i \rangle = \bar{u}_N \left[ F_1(q^2) \gamma^\mu + \frac{i \sigma^{\mu\nu} q_\nu}{2m_N} F_2(q^2) \right] u_N, \quad (4.10)$$

$$\langle f | \bar{Q} T^a \gamma^\mu \gamma_5 Q | i \rangle = \bar{u}_N \left[ F_A(q^2) \gamma^\mu \gamma_5 + \frac{\gamma_5 q^\mu}{m_N} F_P(q^2) \right] u_N, \quad (4.11)$$

where  $M_N = (m_p + m_n)/2$  is the averaged nucleon mass,  $q^2 = (p_f - p_i)^2 = (p_e - p_\chi)^2$  is the squared momentum transfer. In general the form factors are functions of  $q^2$ . Here we consider only the case of that the momentum transfer is negligible, *i.e.*,  $q^2 \rightarrow 0$ , and the form factors reduce to following constants [77],

$$F_1(0) = 1, \quad F_2(0) \simeq 3.706, \quad (4.12)$$

$$F_A(0) = -1.2694 \pm 0.0028, \quad F_P(0) = \frac{2m_N^2}{m_\pi^2} F_A(0), \quad (4.13)$$

where  $m_\pi$  is the mass of the  $\pi$ -meson. Using the matrix elements given in Eq. (4.10) and Eq. (4.11), the averaged squared amplitudes at the nucleon level can be calculated straightforwardly. The full results are relatively complex, and given in the Appendix A. However, the amplitudes in the limit of vanishing threshold, (*i.e.*,  $m_{th}^{\beta^-} \rightarrow 0$  and  $m_e \rightarrow 0$  which means at the nucleon level  $m_p \approx m_n = m_N$ ,  $m_e \approx 0$  and  $E_e \approx m_\chi$ ), can encapsulate some basic properties of the transitions probability, and are given as follows,

$$|\overline{\mathcal{M}_V}|_{m_{th}^{\beta^-} \rightarrow 0}^2 \approx \frac{m_N^4}{\Lambda_V^4} \left[ 4F_1^2 \frac{(m_N + m_\chi)m_\chi^2}{m_N^3} + 2(F_1 F_2 + F_2^2) \frac{m_\chi^3}{m_N^3} \right], \quad (4.14)$$

$$|\overline{\mathcal{M}_A}|_{m_{th}^{\beta^-} \rightarrow 0}^2 \approx \frac{m_N^4}{\Lambda_A^4} \left[ 4F_A^2 \frac{(3m_N + m_\chi)m_\chi^2}{m_N^3} - 4F_P^2 \frac{m_\chi^2(m_N + m_\chi)(m_\chi - E_e)}{m_N^5} \right]. \quad (4.15)$$

One can clearly see that in this limit the terms proportional to  $F_1^2$  ( $F_A^2$ ) is suppressed by a factor of  $m_\chi^2/m_N^2$  for the (axial-) vector operator. Furthermore, for the vector operator, the terms proportional to  $F_1 F_2$  and  $F_2^2$  are suppressed by a factor of  $m_\chi^3/m_N^3$ . Hence for the vector operator the major contribution comes from the nucleon level vector current. On the other hand, for the axial-vector operator, the contribution proportional to  $F_P^2$  is nearly zero in the limit  $E_e \rightarrow m_\chi$ , and particularly the interference (the term proportional to  $F_A F_P$ ) vanishes completely. Therefore, the transition rate is essentially subjected to the nucleon level axial-vector current.

Properties of the amplitude can affect the transition rate because of selection rules. Since angular momentum conservation, the daughter nucleus are generally produced in an excited state. For small momentum transfers, the transition rates are conventionally divided into two general categories: the Fermi transitions in which spin angular momentum of the nucleus does not change ( $\Delta I_F = 0$ ), and the Gamow-Teller transitions in which spin angular momentum of the nucleus receives non-trivial contributions from the leptonic charged current  $\Delta I_{GT} = \pm 1$ . In general, contributions to the Fermi transitions and the Gamow-Teller transitions are non-trivial combinations of the various terms associated with

different form factors [87]. However, in the limit  $q^2 \rightarrow 0$ , the connection is much simplified. The Fermi and Gamow-Teller amplitudes are directly related to the vector and axial-vector currents, respectively. Here we study projected sensitivities of the experiments listed in the Tabel 2, which have better sensitivities because of larger exposure [17]. The corresponding

Experiment	Taget	Exposure
Super-Kamiokande [88]	H <sub>2</sub> O	$1.71 \times 10^5$ t yr
XENONnT [89]	Liquid Xe	1.09 t yr
PandaX-4T [90]	Liquid Xe	0.55 t yr
Borexino [91]	C <sub>6</sub> H <sub>3</sub> (CH <sub>3</sub> ) <sub>3</sub>	817 t yr

**Table 2.** *Experiments considered here to study projected sensitivities by using the induced  $\beta^-$  decay.*

lowest thresholds (have the maximum sensitivities) of the selected isotopes are given in the Table 3.

Process	Isotope (Abundance)	$\Delta I = 0$	$\Delta I = \pm 1$
${}^A_6\text{C} \rightarrow {}^A_7\text{N}$	${}^{12}_6\text{C}$ (98.89%)	18.3 MeV	17.3 MeV
	${}^{13}_6\text{C}$ (1.11%)	2.22 MeV	5.7 MeV
${}^A_8\text{O} \rightarrow {}^A_9\text{F}$	${}^{16}_8\text{O}$ (99.756%)	16.4 MeV	16.4 MeV
	${}^{17}_8\text{O}$ (0.039%)	2.76 MeV	3.75 MeV
	${}^{18}_8\text{O}$ (0.205%)	2.70 MeV	1.65 MeV
${}^A_{54}\text{Xe} \rightarrow {}^A_{55}\text{Cs}$	${}^{126}_{54}\text{Xe}$ (28.4%)	1.19 MeV	1.33 MeV
	${}^{131}_{54}\text{Xe}$ (21.2%)	0.57 MeV	0.355 MeV
	${}^{134}_{54}\text{Xe}$ (10.4%)	2.23 MeV	0.49 MeV
	${}^{136}_{54}\text{Xe}$ (8.8%)	1.09 MeV	1.06 MeV

**Table 3.** *The lowest thresholds of the induced  $\beta^-$  decays.*

Sensitivities of the current experiments are estimated by requiring at least 10 events, and the results are shown in the Fig. 13 (a) and (b) for the vector and axial-vector operators, respectively. For comparison, the expected exclusion limits at 95% C.L. at the LHC13 (cyan), LHC14 (fuchsia) and LHC25 (orange) are also shown. And the constraints at the LHC are obtained by combining all the three processes: mono- $e^\pm$  production, and associated

productions of the  $e^\pm + \gamma/j$  with missing energy. One can see that the direct detection experiments are sensitive to different parameter space due to the different isotopes. In our interested range ( $m_\chi < 10$  MeV) The XENONnT experiment can give the most strongest constraints. However, one can also see that those regions are already covered by the current data at the LHC13<sup>1</sup>. Hence the hadron collider is very promising to search for signals of the four fermion contact interactions involving a dark fermion and a charged lepton. The Super-Kamiokande experiment become more pronounced when  $m_\chi \geq 16.4$  MeV (threshold of the induced  $\beta^-$  decay of the isotope  $^{16}_8\text{O}$ ). However, it beyonds the typical binding energy of the nucleus, and the other multiple correlated signals which do not rely on the nuclear recoils can appear [17, 93]. For instances, emissions of energetic electron/positron and photon, recoil and another  $\beta$  decay of the daughter nucleus. Here we do not intend to study details of these signals, but we stress that inclusion of these signals may give much stronger bounds, and hence comparable to the collider searches.

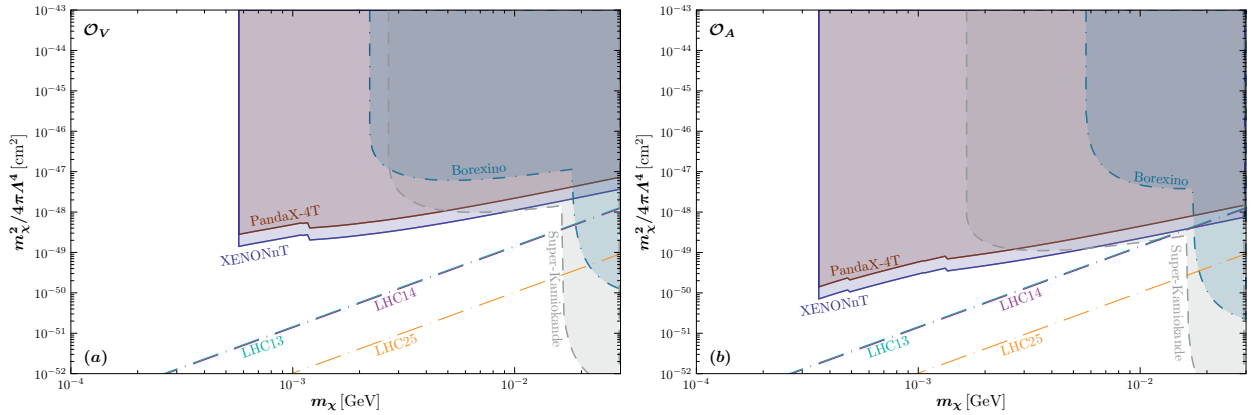


**Figure 13.** The expected constraints from a dedicated search for induced  $\beta^-$  transitions at Super-Kamiokande (gray), XENONnT (blue), PandaX-4T (brown), and Borexino (midnight blue). The expected exclusion limits at 95% C.L. at the LHC13 (cyan), LHC14 (fuchsia) and LHC25 (orange) are also shown. The constraints at the LHC are obtained by combining all the three processes: mono- $e^\pm$  production, and associated productions of the  $e^\pm + \gamma/j$  with missing energy. The **left** and **right** panel stand for the vector and axial-vector operators, respectively.

## 4.2 Induced $\beta^+$ Decay

The nucleus can also undergo induced  $\beta^+$  decay [78]. Since the Pauli Blocking effects in  $\beta^+$  decays of heavy isotopes, the transitions probability into ground state or lowest lying excited states of the daughter nucleus is heavily suppressed. Furthermore, there is no detailed analysis of the favored transitions in the literature, except for the induced  $\beta^+$  decays for Hydrogen [17]. Hence, here we consider only the induced  $\beta^+$  decays for Hydrogen [78],

$$\bar{\chi} + {}^1_1\text{H} \rightarrow n + e^+, \quad (4.16)$$

which has a threshold of 1.8 MeV. Here we consider only the Super-Kamiokande and Borexino experiments, which contain the Hydrogen exposures given in the Table 2. The Super-

<sup>1</sup>In contrast, the data with center of mass energy  $\sqrt{s} = 8$  TeV gives a much weaker bound,  $\Lambda \leq 4.5$  TeV which was estimated in Ref. [17] using the data in the Ref. [92]



Kamiokande experiment has a detection threshold of 70 keV, hence it can probe the dark fermion down to a kinematic threshold of 1.87 MeV. While the Borexino experiment has a detection threshold of 3.5 MeV, and hence it can probe the dark fermion down to a threshold of 5.3 MeV.

The matrix element and decay rate can be easily calculated from the induced  $\beta^-$  decay with the replacement  $n \leftrightarrow p$ . The expected exclusion limits are obtained by requiring at least 10 events. And the results are shown in the Fig. 14 (a) and (b) for the vector and axial vector operators, respectively. Since the induced  $\beta^+$  decays have relatively large thresholds, it provides a complementarity to the induced  $\beta^-$  decay searches. On the other hand, one can also see that the LHC constraints are weaker in parts of the parameter space than the bounds obtained from the induced  $\beta^+$  decay. This is completely different from the case of the induced  $\beta^-$  decay, where the constraints from the LHC are stronger in almost whole of the parameter space. In this sense, the collider searches and induced  $\beta^\pm$  decays are complementary in probing the dark fermion.

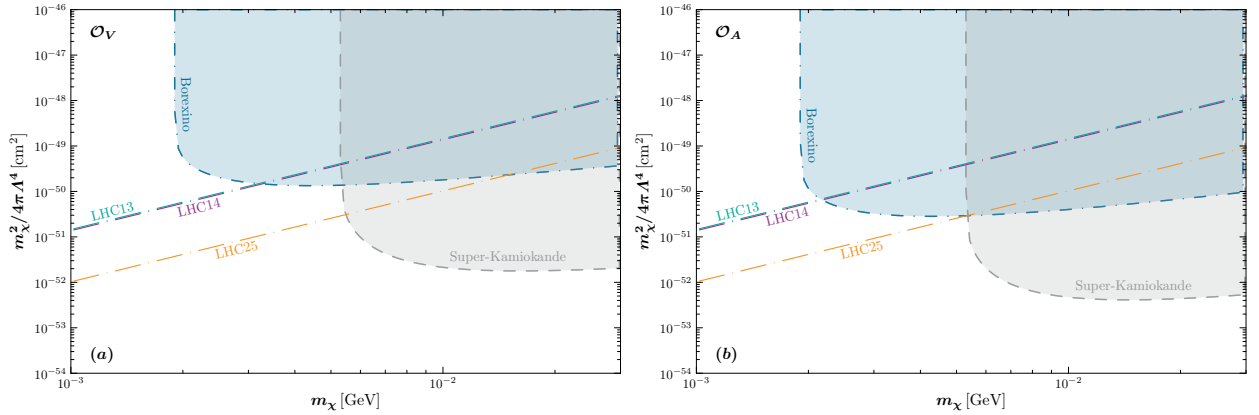


**Figure 14.** The expected constraints from a dedicated search for induced  $\beta^+$  transitions at Super-Kamiokande (gray) and Borexino (midnight blue). The expected exclusion limits at 95% C.L. at the LHC13 (cyan), LHC14 (fuchsia) and LHC25 (orange) are also shown. The constraints at the LHC are obtained by combining all the three processes: mono- $e^\pm$  production, and associated productions of the  $e^\pm + \gamma/j$  with missing energy. The **left** and **right** panel stand for the vector and axial-vector operators, respectively.

## 5 Conclusion

For a fermionic dark particle, the effective interaction with matter particles at the lowest order are simply described by the four fermion contact operators. Here we focus on the operators involving a dark fermion, a charged lepton and a quark pair, which are defined explicitly in Eq. (2.1). And we studied signatures of these operators at the LHC and detect detection experiments.

At the LHC, we show that, the mono-electron production is a powerful probe of the four fermion contact couplings. This is simply due to that the irreducible background dominantly comes from resonant decay of the charged gauge bosons  $W^\pm$ , and hence backgrounds can be dramatically reduced by a proper kinematic cut on the transverse mass. We also studied

associated productions of an electron and a photon/jet with missing energy. Since the total cross sections are suppressed by a factor of  $\alpha_{\text{EM}}$  and  $\alpha_s$ , respectively. The corresponding exclusion limits are weaker than the one from the mono- $e^\pm$  production. However, those processes provides more observables, and correlations between these observables may be used to distinguish structures of the signal operators. Furthermore, by combining all the three channels, the exclusion limits can be enhanced. For the (axial)-vector operators, using the current data at the LHC with  $\sqrt{s} = 13 \text{ TeV}$  the combined lower bounds on the energy scales are  $\Lambda_{V/A} \geq 12.1 \text{ TeV}$  for a massless dark fermion. Furthermore, in view of that the signal cross sections grow with center of mass energy  $\sqrt{\hat{s}}$ , future sensitivities at the LHC with  $\sqrt{s} = 14 \text{ TeV}$  and  $25 \text{ TeV}$  are also studied.

For the direct detection experiments, by matching the operators at quark level and hadron level, we show that the vector and axial-vector currents comes into play separately (it also depends on parameterization of the four fermion contact operator). We focus on the specific induced beta decay for probing the signals. While the vector current undergoes Fermi transitions, the Gamow-Teller transitions happens for the axial-vector operator. For the induced  $\beta^-$  decay, the expected constraints are studied for Super-Kamiokande, XENONnT, PandaX-4T and Borexino experiments which have better sensitivities in their own parameter space. For the induced  $\beta^+$  decay, only the Super-Kamiokande and Borexino experiments are considered for the transition  $\bar{\chi} + {}^1_1\text{H} \rightarrow n + e^+$ . We show that the induced  $\beta^+$  decay can provide better sensitivities in case of that mass of the dark fermion is relatively large, say  $m_\chi > 1.8 \text{ MeV}$  (threshold of the above transition).

By comparing the constraints from the LHC we shown that the collider search can provide better sensitivities than the one of the induced  $\beta^-$  decay in almost whole of the parameter space as shown in the Fig. 13. In contrast, the induced  $\beta^+$  decay is more sensitive than the collider search for a relatively heavy dark fermion, as shown in the Fig. 14. In our analysis of the induced beta decay, we have assumed that  $m_\chi < 10 \text{ MeV}$ , the typical binding energy of the nucleus. Beyond this value, other multiple correlated signals which do not rely on the nuclear recoils can appear [17, 93]. For instances, emissions of energetic electron/positron and photon, recoil and another  $\beta$  decay of the daughter nucleus. We did not study details of these signals, but we stress on that inclusion of these signals may lead to complementarity in the whole parameter space between the collider searches and detect detections.

## A Nucleon Level Squared Amplitudes

The averaged squared amplitudes at the nucleon level are given as,

$$\begin{aligned}
& \overline{|\mathcal{M}_V|} \\
&= \frac{m_n^4}{\Lambda_V^4} \left\{ F_1^2 \left[ \left( \frac{8m_\chi^2}{m_n^3} + \frac{4m_\chi(2m_n - m_p)}{m_n^3} \right) p_e - \frac{4m_\chi}{m_n^3} p_e^2 \right] \right. \\
&+ F_2^2 \left[ \frac{4m_\chi^4 + 2m_\chi^2(3m_n + m_p)^2 + 2m_\chi(m_n^2 - m_p^2)(5m_n + 3m_p) + 12m_\chi^3 m_n}{m_n^3(m_n + m_p)^2} p_e \right. \\
&- \left. \frac{8m_\chi^3 m_n + 16m_\chi^2 m_n^2 + m_\chi(14m_n^3 + 8m_n^2 m_p + 2m_n m_p^2)}{m_n^4(m_n + m_p)^2} p_e^2 + \frac{4m_\chi^2 + 4m_\chi m_n}{m_n^3(m_n + m_p)^2} p_e^3 \right] \\
&- \left. \frac{2F_1 F_2 m_\chi m_n p_e}{m_n^4(m_n + m_p)} \left[ 2m_\chi^2 - m_n^2 + m_p^2 + m_\chi(m_n - 9m_p - 2p_e) - m_n p_e + 7m_p p_e \right] \right\}, \quad (\text{A.1})
\end{aligned}$$

$$\begin{aligned}
& \overline{|\mathcal{M}_A|} \\
&= \frac{m_n^4}{\Lambda_A^4} \left\{ F_A^2 \left[ \frac{8m_\chi^2 + 4m_\chi(2m_n + m_p)}{m_n^3} p_e - \frac{4m_\chi}{m_n^3} p_e^2 \right] \right. \\
&- F_P^2 \left[ \left( \frac{16m_\chi^4 + 16m_\chi^3(2m_n - m_p) + 8m_\chi^2(3m_n^2 - 2m_n m_p - m_p^2)}{m_n^3(m_n + m_p)^2} \right. \right. \\
&+ \left. \frac{8m_\chi(m_n^3 - m_n^2 m_p - m_n m_p^2 + m_p^3)}{m_n^3(m_n + m_p)^2} \right) p_e + \left( \frac{-32m_\chi^3 - 16m_\chi^2(3m_n - m_p)}{m_n^3(m_n + m_p)^2} \right. \\
&+ \left. \left. \frac{8m_\chi(-3m_n^2 + 2m_n m_p + m_p^2)}{m_n^3(m_n + m_p)^2} \right) p_e^2 + \frac{16m_\chi(m_\chi + m_p)}{m_n^3(m_n + m_p)^2} p_e^3 \right] \right\}. \quad (\text{A.2})
\end{aligned}$$

## Acknowledgments

K.M. was supported by the Innovation Capability Support Program of Shaanxi (Program No. 2021KJXX-47).

## References

- [1] G. Bertone, D. Hooper and J. Silk, *Particle dark matter: Evidence, candidates and constraints*, *Phys. Rept.* **405** (2005) 279 [[hep-ph/0404175](#)].
- [2] B.-L. Young, *A survey of dark matter and related topics in cosmology*, *Front. Phys. (Beijing)* **12** (2017) 121201.
- [3] A. Arbey and F. Mahmoudi, *Dark matter and the early Universe: a review*, *Prog. Part. Nucl. Phys.* **119** (2021) 103865 [[2104.11488](#)].

- [4] R.K. Leane, *Indirect Detection of Dark Matter in the Galaxy*, in *3rd World Summit on Exploring the Dark Side of the Universe*, pp. 203–228, 2020 [[2006.00513](#)].
- [5] T.R. Slatyer, *Les Houches Lectures on Indirect Detection of Dark Matter*, *SciPost Phys. Lect. Notes* **53** (2022) 1 [[2109.02696](#)].
- [6] A. Bouquet, P. Salati and J. Silk,  *$\gamma$ -Ray Lines as a Probe for a Cold Dark Matter Halo*, *Phys. Rev. D* **40** (1989) 3168.
- [7] E.A. Baltz and L. Bergstrom, *Detection of leptonic dark matter*, *Phys. Rev. D* **67** (2003) 043516 [[hep-ph/0211325](#)].
- [8] I. John and T. Linden, *Cosmic-Ray Positrons Strongly Constrain Leptophilic Dark Matter*, *JCAP* **12** (2021) 007 [[2107.10261](#)].
- [9] X.-J. Bi, X.-G. He and Q. Yuan, *Parameters in a class of leptophilic models from PAMELA, ATIC and FERMI*, *Phys. Lett. B* **678** (2009) 168 [[0903.0122](#)].
- [10] A. Ibarra, A. Ringwald, D. Tran and C. Weniger, *Cosmic Rays from Leptophilic Dark Matter Decay via Kinetic Mixing*, *JCAP* **08** (2009) 017 [[0903.3625](#)].
- [11] L. Roszkowski, E.M. Sessolo and S. Trojanowski, *WIMP dark matter candidates and searches—current status and future prospects*, *Rept. Prog. Phys.* **81** (2018) 066201 [[1707.06277](#)].
- [12] J. de Dios Zornoza, *Review on Indirect Dark Matter Searches with Neutrino Telescopes*, *Universe* **7** (2021) 415.
- [13] C.R. Argüelles, E.A. Becerra-Vergara, J.A. Rueda and R. Ruffini, *Fermionic Dark Matter: Physics, Astrophysics, and Cosmology*, *Universe* **9** (2023) 197 [[2304.06329](#)].
- [14] M.W. Goodman and E. Witten, *Detectability of Certain Dark Matter Candidates*, *Phys. Rev. D* **31** (1985) 3059.
- [15] B. Batell, P. deNiverville, D. McKeen, M. Pospelov and A. Ritz, *Leptophobic Dark Matter at Neutrino Factories*, *Phys. Rev. D* **90** (2014) 115014 [[1405.7049](#)].
- [16] J.A. Dror, G. Elor and R. McGehee, *Directly Detecting Signals from Absorption of Fermionic Dark Matter*, *Phys. Rev. Lett.* **124** (2020) 18 [[1905.12635](#)].
- [17] J.A. Dror, G. Elor and R. McGehee, *Absorption of Fermionic Dark Matter by Nuclear Targets*, *JHEP* **02** (2020) 134 [[1908.10861](#)].
- [18] J.A. Dror, G. Elor, R. McGehee and T.-T. Yu, *Absorption of sub-MeV fermionic dark matter by electron targets*, *Phys. Rev. D* **103** (2021) 035001 [[2011.01940](#)].
- [19] A. Mitridate, K. Pardo, T. Trickle and K.M. Zurek, *Effective field theory for dark matter absorption on single phonons*, *Phys. Rev. D* **109** (2024) 015010 [[2308.06314](#)].
- [20] J. Liu, X. Chen and X. Ji, *Current status of direct dark matter detection experiments*, *Nature Phys.* **13** (2017) 212 [[1709.00688](#)].
- [21] J. Billard et al., *Direct detection of dark matter—APPEC committee report\**, *Rept. Prog. Phys.* **85** (2022) 056201 [[2104.07634](#)].
- [22] O. Buchmueller, M.J. Dolan, S.A. Malik and C. McCabe, *Characterising dark matter searches at colliders and direct detection experiments: Vector mediators*, *JHEP* **01** (2015) 037 [[1407.8257](#)].

- [23] LZ collaboration, *First Dark Matter Search Results from the LUX-ZEPLIN (LZ) Experiment*, *Phys. Rev. Lett.* **131** (2023) 041002 [[2207.03764](#)].
- [24] A. Boveia and C. Doglioni, *Dark Matter Searches at Colliders*, *Ann. Rev. Nucl. Part. Sci.* **68** (2018) 429 [[1810.12238](#)].
- [25] S. Gori et al., *Dark Sector Physics at High-Intensity Experiments*, [2209.04671](#).
- [26] T. Lagouri, *Review on Higgs Hidden–Dark Sector Physics at High-Energy Colliders*, *Symmetry* **14** (2022) 1299.
- [27] B. Penning, *The pursuit of dark matter at colliders—an overview*, *J. Phys. G* **45** (2018) 063001 [[1712.01391](#)].
- [28] S.-F. Ge, K. Ma, X.-D. Ma and J. Sheng, *Associated production of neutrino and dark fermion at future lepton colliders*, *JHEP* **11** (2023) 190 [[2306.00657](#)].
- [29] A. Belyaev, E. Bertuzzo, C. Caniu Barros, O. Eboli, G. Grilli Di Cortona, F. Iocco et al., *Interplay of the LHC and non-LHC Dark Matter searches in the Effective Field Theory approach*, *Phys. Rev. D* **99** (2019) 015006 [[1807.03817](#)].
- [30] H. Dreiner, D. Schmeier and J. Tattersall, *Contact Interactions Probe Effective Dark Matter Models at the LHC*, *EPL* **102** (2013) 51001 [[1303.3348](#)].
- [31] S. Belwal, M. Drees and J.S. Kim, *Analysis of the Bounds on Dark Matter Models from Monojet Searches at the LHC*, *Phys. Rev. D* **98** (2018) 055017 [[1709.08545](#)].
- [32] S.-F. Ge, X.-G. He, X.-D. Ma and J. Sheng, *Revisiting the fermionic dark matter absorption on electron target*, *JHEP* **05** (2022) 191 [[2201.11497](#)].
- [33] R. Cepedello, F. Esser, M. Hirsch and V. Sanz, *SMEFT goes dark: Dark Matter models for four-fermion operators*, *JHEP* **09** (2023) 081 [[2302.03485](#)].
- [34] A. Falkowski and K. Mimouni, *Model independent constraints on four-lepton operators*, *JHEP* **02** (2016) 086 [[1511.07434](#)].
- [35] E. Bernreuther, J. Horak, T. Plehn and A. Butter, *Actual Physics behind Mono-X*, *SciPost Phys.* **5** (2018) 034 [[1805.11637](#)].
- [36] A. Krovi, I. Low and Y. Zhang, *Broadening Dark Matter Searches at the LHC: Mono-X versus Darkonium Channels*, *JHEP* **10** (2018) 026 [[1807.07972](#)].
- [37] S.P. Liew, M. Papucci, A. Vichi and K.M. Zurek, *Mono-X Versus Direct Searches: Simplified Models for Dark Matter at the LHC*, *JHEP* **06** (2017) 082 [[1612.00219](#)].
- [38] S. Bhattacharya, P. Ghosh, J. Lahiri and B. Mukhopadhyaya, *Mono-X signal and two component dark matter: new distinction criteria*, [2211.10749](#).
- [39] T. Li, J. Liao and R.-J. Zhang, *Dark magnetic dipole property in fermionic absorption by nucleus and electrons*, *JHEP* **05** (2022) 071 [[2201.11905](#)].
- [40] T.D. Lee and C.-N. Yang, *Question of Parity Conservation in Weak Interactions*, *Phys. Rev.* **104** (1956) 254.
- [41] R.J. Hill and M.P. Solon, *Universal behavior in the scattering of heavy, weakly interacting dark matter on nuclear targets*, *Phys. Lett. B* **707** (2012) 539 [[1111.0016](#)].
- [42] M.T. Frandsen, U. Haisch, F. Kahlhoefer, P. Mertsch and K. Schmidt-Hoberg, *Loop-induced*

- dark matter direct detection signals from gamma-ray lines, *JCAP* **10** (2012) 033 [[1207.3971](#)].
- [43] L. Vecchi, *WIMPs and Un-Naturalness*, [1312.5695](#).
  - [44] A. Crivellin, F. D'Eramo and M. Procura, *New Constraints on Dark Matter Effective Theories from Standard Model Loops*, *Phys. Rev. Lett.* **112** (2014) 191304 [[1402.1173](#)].
  - [45] F. D'Eramo and M. Procura, *Connecting Dark Matter UV Complete Models to Direct Detection Rates via Effective Field Theory*, *JHEP* **04** (2015) 054 [[1411.3342](#)].
  - [46] F. D'Eramo, B.J. Kavanagh and P. Panci, *You can hide but you have to run: direct detection with vector mediators*, *JHEP* **08** (2016) 111 [[1605.04917](#)].
  - [47] F. Bishara, J. Brod, B. Grinstein and J. Zupan, *From quarks to nucleons in dark matter direct detection*, *JHEP* **11** (2017) 059 [[1707.06998](#)].
  - [48] G. Busoni, A. De Simone, E. Morgante and A. Riotto, *On the Validity of the Effective Field Theory for Dark Matter Searches at the LHC*, *Phys. Lett. B* **728** (2014) 412 [[1307.2253](#)].
  - [49] G. Busoni, A. De Simone, J. Gramling, E. Morgante and A. Riotto, *On the Validity of the Effective Field Theory for Dark Matter Searches at the LHC, Part II: Complete Analysis for the s-channel*, *JCAP* **06** (2014) 060 [[1402.1275](#)].
  - [50] G. Busoni, A. De Simone, T. Jacques, E. Morgante and A. Riotto, *On the Validity of the Effective Field Theory for Dark Matter Searches at the LHC Part III: Analysis for the t-channel*, *JCAP* **09** (2014) 022 [[1405.3101](#)].
  - [51] W. Abdallah, J. Fiaschi, S. Khalil and S. Moretti, *Mono-jet, -photon and -Z signals of a supersymmetric ( $B - L$ ) model at the Large Hadron Collider*, *JHEP* **02** (2016) 157 [[1510.06475](#)].
  - [52] G.G. da Silveira and M.S. Mateus, *Investigation of spin-dependent dark matter in mono-photon production at high-energy colliders*, [2308.03680](#).
  - [53] E. Gabrielli, M. Heikinheimo, B. Mele and M. Raidal, *Dark photons and resonant monophoton signatures in Higgs boson decays at the LHC*, *Phys. Rev. D* **90** (2014) 055032 [[1405.5196](#)].
  - [54] Y. Gershtein, F. Petriello, S. Quackenbush and K.M. Zurek, *Discovering hidden sectors with mono-photon  $Z'$  searches*, *Phys. Rev. D* **78** (2008) 095002 [[0809.2849](#)].
  - [55] Y. Hiçiyilmaz, L. Selbuz and C.S. Ün, *Monophoton events with light Higgs bosons in the secluded UMSSM*, *Phys. Rev. D* **108** (2023) 075002 [[2303.05502](#)].
  - [56] J. Kawamura, *Mono-Z/W Signal from Nearly Degenerate Higgsinos at the LHC*, *LHEP* **2023** (2023) 337.
  - [57] D. Yang and Q. Li, *Probing the Dark Sector through Mono-Z Boson Leptonic Decays*, *JHEP* **02** (2018) 090 [[1711.09845](#)].
  - [58] W. Abdallah, A. Hammad, S. Khalil and S. Moretti, *Dark matter spin characterization in mono-Z channels*, *Phys. Rev. D* **100** (2019) 095006 [[1907.08358](#)].
  - [59] J.M. No, *Looking through the pseudoscalar portal into dark matter: Novel mono-Higgs and mono-Z signatures at the LHC*, *Phys. Rev. D* **93** (2016) 031701 [[1509.01110](#)].
  - [60] N.F. Bell, J.B. Dent, A.J. Galea, T.D. Jacques, L.M. Krauss and T.J. Weiler, *Searching for Dark Matter at the LHC with a Mono-Z*, *Phys. Rev. D* **86** (2012) 096011 [[1209.0231](#)].



- [61] A. Alves and K. Sinha, *Searches for Dark Matter at the LHC: A Multivariate Analysis in the Mono-Z Channel*, *Phys. Rev. D* **92** (2015) 115013 [[1507.08294](#)].
- [62] N. Wan, N. Li, B. Zhang, H. Yang, M.-F. Zhao, M. Song et al., *Searches for Dark Matter via Mono-W Production in Inert Doublet Model at the LHC*, *Commun. Theor. Phys.* **69** (2018) 617.
- [63] N.F. Bell, Y. Cai and R.K. Leane, *Mono-W Dark Matter Signals at the LHC: Simplified Model Analysis*, *JCAP* **01** (2016) 051 [[1512.00476](#)].
- [64] J. Claude, M. Dutra and S. Godfrey, *Probing feebly interacting dark matter with monojet searches*, *Phys. Rev. D* **107** (2023) 075006 [[2208.09422](#)].
- [65] A. Belyaev, T.R. Fernandez Perez Tomei, P.G. Mercadante, C.S. Moon, S. Moretti, S.F. Novaes et al., *Advancing LHC probes of dark matter from the inert two-Higgs-doublet model with the monojet signal*, *Phys. Rev. D* **99** (2019) 015011 [[1809.00933](#)].
- [66] Y. Bai, J. Bourbeau and T. Lin, *Dark matter searches with a mono-Z' jet*, *JHEP* **06** (2015) 205 [[1504.01395](#)].
- [67] J. Alwall, R. Frederix, S. Frixione, V. Hirschi, F. Maltoni, O. Mattelaer et al., *The automated computation of tree-level and next-to-leading order differential cross sections, and their matching to parton shower simulations*, *JHEP* **07** (2014) 079 [[1405.0301](#)].
- [68] R. Frederix, S. Frixione, V. Hirschi, D. Pagani, H.S. Shao and M. Zaro, *The automation of next-to-leading order electroweak calculations*, *JHEP* **07** (2018) 185 [[1804.10017](#)].
- [69] A. Alloul, N.D. Christensen, C. Degrande, C. Duhr and B. Fuks, *FeynRules 2.0 - A complete toolbox for tree-level phenomenology*, *Comput. Phys. Commun.* **185** (2014) 2250 [[1310.1921](#)].
- [70] C. Degrande, C. Duhr, B. Fuks, D. Grellscheid, O. Mattelaer and T. Reiter, *UFO - The Universal FeynRules Output*, *Comput. Phys. Commun.* **183** (2012) 1201 [[1108.2040](#)].
- [71] ATLAS collaboration, *Search for a heavy charged boson in events with a charged lepton and missing transverse momentum from pp collisions at  $\sqrt{s} = 13$  TeV with the ATLAS detector*, *Phys. Rev. D* **100** (2019) 052013 [[1906.05609](#)].
- [72] ATLAS collaboration, *Search for a new heavy gauge boson resonance decaying into a lepton and missing transverse momentum in  $36 \text{ fb}^{-1}$  of pp collisions at  $\sqrt{s} = 13$  TeV with the ATLAS experiment*, *Eur. Phys. J. C* **78** (2018) 401 [[1706.04786](#)].
- [73] CMS collaboration, *Search for high-mass resonances in final states with a lepton and missing transverse momentum at  $\sqrt{s} = 13$  TeV*, *JHEP* **06** (2018) 128 [[1803.11133](#)].
- [74] CMS collaboration, *Search for supersymmetry in events with a photon, a lepton, and missing transverse momentum in proton-proton collisions at  $\sqrt{s} = 13$  TeV*, *JHEP* **01** (2019) 154 [[1812.04066](#)].
- [75] ATLAS collaboration, *Search for quantum black hole production in lepton+jet final states using proton-proton collisions at  $\sqrt{s} = 13$  TeV with the ATLAS detector*, [2307.14967](#).
- [76] X. Cid Vidal et al., *Report from Working Group 3: Beyond the Standard Model physics at the HL-LHC and HE-LHC*, *CERN Yellow Rep. Monogr.* **7** (2019) 585 [[1812.07831](#)].
- [77] J.A. Formaggio and G.P. Zeller, *From eV to EeV: Neutrino Cross Sections Across Energy Scales*, *Rev. Mod. Phys.* **84** (2012) 1307 [[1305.7513](#)].



- [78] P. Vogel and J.F. Beacom, *Angular distribution of neutron inverse beta decay, anti-neutrino( $e$ ) +  $p \rightarrow e + n$* , *Phys. Rev. D* **60** (1999) 053003 [[hep-ph/9903554](#)].
- [79] E. Del Nobile, *The Theory of Direct Dark Matter Detection: A Guide to Computations*, [2104.12785](#).
- [80] J.D. Jackson, S.B. Treiman and H.W. Wyld, *Possible tests of time reversal invariance in Beta decay*, *Phys. Rev.* **106** (1957) 517.
- [81] M. Avila-Aoki and A. Garcia, *Scalar, pseudoscalar and tensorial electromagnetic corrections to the Beta decay rate of the neutron*, .
- [82] P. Langacker, M.-x. Luo and A.K. Mann, *High precision electroweak experiments: A Global search for new physics beyond the standard model*, *Rev. Mod. Phys.* **64** (1992) 87.
- [83] M. Anholm, *A precision search for exotic scalar and tensor couplings in the beta decay of spin-polarized  $^{37}\text{K}$* , Ph.D. thesis, Manitoba U., 2023.
- [84] M. Beck, W. Heil, C. Schmidt, S. Baeßler, F. Glück, G. Konrad et al., *Reanalysis of the  $\beta-\nu^-e$  Angular Correlation Measurement from the aSPECT Experiment with New Constraints on Fierz Interference*, *Phys. Rev. Lett.* **132** (2024) 102501 [[2308.16170](#)].
- [85] H. Saul, C. Roick, H. Abele, H. Mest, M. Klopff, A. Petukhov et al., *Limit on the Fierz Interference Term  $b$  from a Measurement of the Beta Asymmetry in Neutron Decay*, *Phys. Rev. Lett.* **125** (2020) 112501 [[1911.01766](#)].
- [86] UCNA collaboration, *Improved limits on Fierz interference using asymmetry measurements from the Ultracold Neutron Asymmetry (UCNA) experiment*, *Phys. Rev. C* **101** (2020) 035503 [[1911.05829](#)].
- [87] T. Kuramoto, M. Fukugita, Y. Kohyama and K. Kubodera, *Neutrino Induced Reaction Cross-sections at Intermediate-energies for Chlorine and Water Detectors*, *Nucl. Phys. A* **512** (1990) 711.
- [88] SUPER-KAMIOKANDE collaboration, *Measurement of the neutrino-oxygen neutral-current quasielastic cross section using atmospheric neutrinos at Super-Kamiokande*, *Phys. Rev. D* **99** (2019) 032005 [[1901.05281](#)].
- [89] XENON collaboration, *First Dark Matter Search with Nuclear Recoils from the XENONnT Experiment*, *Phys. Rev. Lett.* **131** (2023) 041003 [[2303.14729](#)].
- [90] PANDAX collaboration, *Search for Dark-Matter–Nucleon Interactions with a Dark Mediator in PandaX-4T*, *Phys. Rev. Lett.* **131** (2023) 191002 [[2308.01540](#)].
- [91] BOREXINO collaboration, *Modulations of the Cosmic Muon Signal in Ten Years of Borexino Data*, *JCAP* **02** (2019) 046 [[1808.04207](#)].
- [92] CMS collaboration, *Search for physics beyond the standard model in final states with a lepton and missing transverse energy in proton-proton collisions at  $\sqrt{s} = 8$  TeV*, *Phys. Rev. D* **91** (2015) 092005 [[1408.2745](#)].
- [93] T. Lasserre, K. Altenmueller, M. Cribier, A. Merle, S. Mertens and M. Vivier, *Direct Search for keV Sterile Neutrino Dark Matter with a Stable Dysprosium Target*, [1609.04671](#).